NOAA Technical Memorandum NWS TDL 66

THE STATE OF THE TECHNIQUES DEVELOPMENT LABORATORY'S BOUNDARY LAYER MODEL: MAY 24, 1977

Techniques Development Laboratory
Silver Spring, Md.
July 1978

noaa NATIONAL OCEANIC AND ATMOSPHERIC ADMINISTRATION / National Weather Service

NOAA TECHNICAL MEMORANDUMS

National Weather Service, Techniques Development Laboratory Series

The primary purpose of the Techniques Development Laboratory of the Office of Systems Development is to translate increases of basic knowledge in meteorology and allied disciplines into improved operating techniques and procedures. To achieve this goal, the laboratory conducts applied research and development aimed at the improvement of diagnostic and prognostic methods for producing weather information. The laboratory performs studies both for the general improvement of prediction methodology used in the National Meteorological Service and for the more effective utilization of weather forecasts by the ultimate user.

NOAA Technical Memorandums in the National Weather Service Techniques Development Laboratory series facilitate rapid distribution of material that may be preliminary in nature and which may be published formally elsewhere at a later date. Publications 1 through 5 are in the former series, Weather Bureau Technical Notes (TN), Techniques Development Laboratory (TDL) Reports; publications 6 through 36 are in the former series, ESSA Technical Memorandums, Weather Bureau Technical Memorandums (WBTM). Beginning with TDL 37, publications are now part of the series NOAA Technical Memorandums National Weather Service (NWS).

Publications listed below are available from the National Technical Information Service, U.S. Department of Commerce, Sills Bldg., 5285 Port Royal Road, Springfield, VA 22161. Prices on request. Order by accession number (given in parentheses). Information on memorandums not listed below can be obtained from Environmental Science Information Center (D822), NOAA, 6009 Executive Boulevard, Rockville, MD 20852.

ESSA Technical Memorandums

WBTM TDL 13 Interim Report on Sea and Swell Forecasting. N. A. Pore and W. S. Richardson, December 1967, 21 pp. (PB-177-038)

WBTM TDL 14 Meteorological Analysis of 1964-65 ICAO Turbulence Data. DeVer Colson, October 1968, 80 pp. (PB-180-268)

WBTM TDL 15 Prediction of Temperature and Dew Point by Three-Dimensional Trajectories. Ronald M. Reap, October 1968, 20 pp. (PB-180-727)

WBTM TDL 16 Objective Visibility Forecasting Techniques Based on Surface and Tower Observations. Donald M. Gales, October 1968, 29 pp. (PB-180-479)

WBTM TDL 17 Second Interim Report on Sea and Swell Forecasting. N. A. Pore and W. S. Richardson, January 1969, 7 pp. plus 10 figures. (PB-182-273)

WBTM TDL 18 Conditional Probabilities of Precipitation Amounts in the Conterminous United States. Donald L. Jorgensen, William H. Klein, and Charles F. Roberts, March 1969, 89 pp. (PB-183-144)

WBTM TDL 19 An Operationally Oriented Small-Scale 500-Millibar Height Analysis Program. Harry R. Glahn and George W. Hollenbaugh, March 1969, 17 pp. (PB-184-111)

WBTM TDL 20 A Comparison of Two Methods of Reducing Truncation Error. Robert J. Bermowitz, May 1969, 7 pp. (PB-184-741)

WBTM TDL 21 Automatic Decoding of Hourly Weather Reports. George W. Hollenbaugh, Harry R. Glahn, and Dale A. Lowry, July 1969, 27 pp. (PB-185-806)

WBTM TDL 22 An Operationally Oriented Objective Analysis Program. Harry R. Glahn, George W. Hollenbaugh, and Dale A. Lowry, July 1969, 20 pp. (PB-186-129)

WBTM TDL 23 An Operational Subsynoptic Advection Model. Harry R. Glahn, Dale A. Lowry, and George W. Hollenbaugh, July 1969, 26 pp. (PB-186-389)

WBTM TDL 24 A Lake Erie Storm Surge Forecasting Technique. William S. Richardson and N. Arthur Pore, August 1969, 23 pp. (PB-185-778)

WBTM TDL 25 Charts Giving Station Precipitation in the Plateau States From 850- and 500-Millibar Lows During Winter. August F. Korte, Donald L. Jorgensen, and William H. Klein, September 1969, 9 pp. plus appendixes A and B. (PB-187-476)

WBTM TDL 26 Computer Forecasts of Maximum and Minimum Surface Temperatures. William H. Klein, Frank Lewis, and George P. Casely, October 1969, 27 pp. plus appendix. (PB-189-105)

WBTM TDL 27 An Operational Method for Objectively Forecasting Probability of Precipitation. Harry R. Glahn and Dale A. Lowry, October 1969, 24 pp. (PB-188-660)

WBTM TDL 28 Techniques for Forecasting Low Water Occurrences at Baltimore and Norfolk. James M. McClelland, March 1970, 34 pp. (PB-191-744)

WBTM TDL 29 A Method for Predicting Surface Winds. Harry R. Glahn, March 1970, 18 pp. (PB-191-745)

WBTM TDL 30 Summary of Selected Reference Material on the Oceanographic Phenomena of Tides, Storm Surges, Waves, and Breakers. N. Arthur Pore, May 1970, 103 pp. (PB-193-449)

WBTM TDL 31 Persistence of Precipitation at 108 Cities in the Conterminous United States. Donald L. Jorgensen and William H. Klein, May 1970, 84 pp. (PB-193-599)

WBTM TDL 32 Computer-Produced Worded Forecasts. Harry R. Glahn, June 1970, 8 pp. (PB-194-262)

(Continued on inside back cover)

NOAA Technical Memorandum NWS TDL 66

THE STATE OF THE TECHNIQUES DEVELOPMENT LABORATORY'S BOUNDARY LAYER MODEL: MAY 24, 1977

P. E. Long
W. A. Shaffer
J. E. Kemper
F. J. Hicks

Techniques Development Laboratory
Silver Spring, Md.
July 1978

UNITED STATES
DEPARTMENT OF COMMERCE
Juanita M. Kreps, Secretary

NATIONAL OCEANIC AND
ATMOSPHERIC ADMINISTRATION
Richard A. Frank, Administrator

National Weather
Service
George P. Cressman, Director

CONTENTS

	Page
Abstract	1
1. Introduction	2
2. Basic Relations	
a. Predictive Equations	6
b. Surface Layer Relations	8
c. K-profiles	10
d. Numerical Methods	11
3. Surface and Physical Effects	
a. Model Terrain	13
b. Surface Roughness	13
c. Soil Thermal Properties	13
d. Surface Energy Balance and Radiation Effects	13
e. The Effects of Terrain-Following Coordinates	20
4. Preparation and Objective Analysis of Initial Data	
a. General	21
b. Data Processing and Error Checking	22
c. Objective Analysis (Mapping)	26
d. Filtering	28
e. Special Processing	29
5. Verification of the Boundary Layer Model's Forecast	
a. Basics	35
b. Wind Analysis	35
c. Temperature Analysis	38
d. Humidity Analysis	38

Page

Acknowledgment 38

References 38

Appendix A: Long Wave Radiation Flux 41

Appendix B: Short Wave Radiation Fluxes 44

Appendix C: Soil Heat Flux 47

Appendix D: Numerical Schemes for Advection and Diffusion . . 50

Appendix E: Surface Layer Relations 54

Appendix F: List of Symbols 56

FIGURES

Figure 1.1. Present forecast area covered by the boundary layer model 3

Figure 1.2. Vertical structure of TDL's 3-dimensional boundary layer model. 4

Figure 1.3. The model solves an energy flux balance to obtain surface values for temperature and humidity. 5

Figure 3.1. The model's terrain is shown contoured at intervals of 100 m. 14

Figure 3.2. Surface roughness, z_o, used in the BLM is contoured at 0.1 m intervals. 15

Figure 3.3. The BLM's surface temperature and humidity are determined through surface energy flux balance.. 16

Figure 3.4. Results of running the one-dimensional model with and without radiative heating due to flux divergences 19

Figure 4.1. Surface (2 m) temperature analysis for 1200 GMT, March 18, 1977 23

Figure 4.2. 50 m temperature analysis contours and observations for 1200 GMT, March 18, 1977 24

Figure 4.3. Response function and filter weights for a cutoff wavelength of $3\Delta x$ 30

Page

Figure 4.4. Surface wind analysis and observations for 1200 GMT, March 18, 1977 31

Figure 4.5. Same as figure 4.4 except level is now 2000 m 32

Figure 4.6. Surface geostrophic wind analysis for 1200 GMT, March 18, 1977 33

Figure 4.7. Same as figure 4.6 except level is now 2000 m 34

Figure 4.8. Marine adjusted surface temperature analysis for 1200 GMT, March 18, 1977 36

Figure 4.9. Marine adjusted and filtered 50 m temperature analysis 37

Figure A.1. Treatment of long wave radiation, including clouds within the boundary layer 43

Figure B.1. Treatment of solar radiation 46

TABLE

Table C.1. Evaluation of the soil heat term for various initial profiles 49

THE STATE OF THE TECHNIQUES DEVELOPMENT LABORATORY'S BOUNDARY LAYER MODEL: MAY 24, 1977

P. E. Long, W. A. Shaffer, J. E. Kemper, and F. J. Hicks
Techniques Development Laboratory
National Weather Service, NOAA
Silver Spring, Md. 20910

ABSTRACT. This report surveys the current physics, numerics, objective analysis, and verification of the Techniques Development Laboratory's atmospheric Boundary Layer Model. The model is semi-operational and can produce daily forecasts extending to 24 hours for wind, temperature, and humidity within the earth's lowest two kilometers. The model's forecast area consists of most of the United States east of the Rocky Mountains and is covered with a computational grid with an 80-km mesh spacing. There are two basic layers in the model in which ten computational levels are imbedded. The surface layer uses Obukhov similarity theory. The transition layer equations are time dependent and draw their lower boundary conditions from the surface layer relations. The surface temperature is computed from an energy flux balance. Radiative heating is included in the temperature calculations above the surface.

The time dependent equations that govern the transition layer are solved with implicit schemes and the splitting method: the horizontal advection equations use linear finite elements while the vertical diffusion equations use finite difference equations with selective damping. A new implicit filter has been devised to help damp shortwave noise.

Radiosonde data are checked and analyzed to give profiles of wind, temperature, and specific humidity at each of the model's 35 x 30 (= 1,050) horizontal grid points. The analysis uses approximately 65 upper air stations. Ship observations help define fields over water areas. Much of the data preparation and analysis consists of careful data checking; special techniques have been developed to assure the quality of the initial fields.

1. INTRODUCTION

This report surveys the state of the Techniques Development Laboratory's (TDL's) atmospheric Boundary Layer Model (BLM) as of May 1977. The survey is clearly too slim to be complete. A full treatment would be tedious and, more important, out of date by the time of its completion. We feel, however, that although the details of the model will almost certainly change, the model is sufficiently advanced that a brief description is warranted.

TDL is now running semi-operationally a large scale atmospheric boundary layer model. The model produces daily forecasts extending to 24 hours for wind, temperature, and humidity within the atmosphere's lowest two kilometers. The forecast area is most of the United States east of the Rocky Mountains (fig. 1.1). It is expected that the model will be instrumental in improving TDL's severe storm forecasts as well as providing guidance for air pollution models.

The computational mesh spacing of the BLM is about 80 km, half that of the National Weather Service's Limited-area Fine Mesh model (LFM). The LFM is a large-scale, free-air primitive equation model that provides the upper boundary conditions to the BLM. Future plans call for the LFM to supply the inflow lateral boundary conditions as well.

The BLM has two physical-mathematical layers containing ten computational levels (fig. 1.2). The lower surface layer, extending from the surface to 50 m, uses Obukhov similarity theory as determined by the empirical profile relationships of Webb (1970) and Businger, et al. (1971). The surface layer's principal function is to obviate the computation of temperature, humidity, and wind at a prohibitive number of levels between the surface and 50 m. Although such a refinement is desirable as a research tool, it is not feasible for an operational model. The surface layer relations provide lower boundary conditions for the upper transition layer ($50 \leq z \leq 2000$ m), as discussed by Shaffer and Long (1973). The surface temperature and humidity are diagnosed through a surface energy balance (fig. 1.3, also see Shaffer, 1978).

The predictive transition layer equations are integrated in time with implicit schemes and the splitting method (Long and Shaffer, 1973). In particular, the horizontal equations of motion are solved with a linear finite-element (chapeau) method (Long and Hicks, 1975; Long and Pepper, 1976). The method is stable and accurate.

In the analysis portion of the model, wind, temperature, dewpoint, and pressure are determined at each of the model's gridpoints, on the basis of radiosonde data. Roughly 50 upper air observations within the grid and another 15 just outside the grid go into the analysis. To extract as much information as is available in the soundings, we use both the mandatory and significant level information. We include surface ship observations

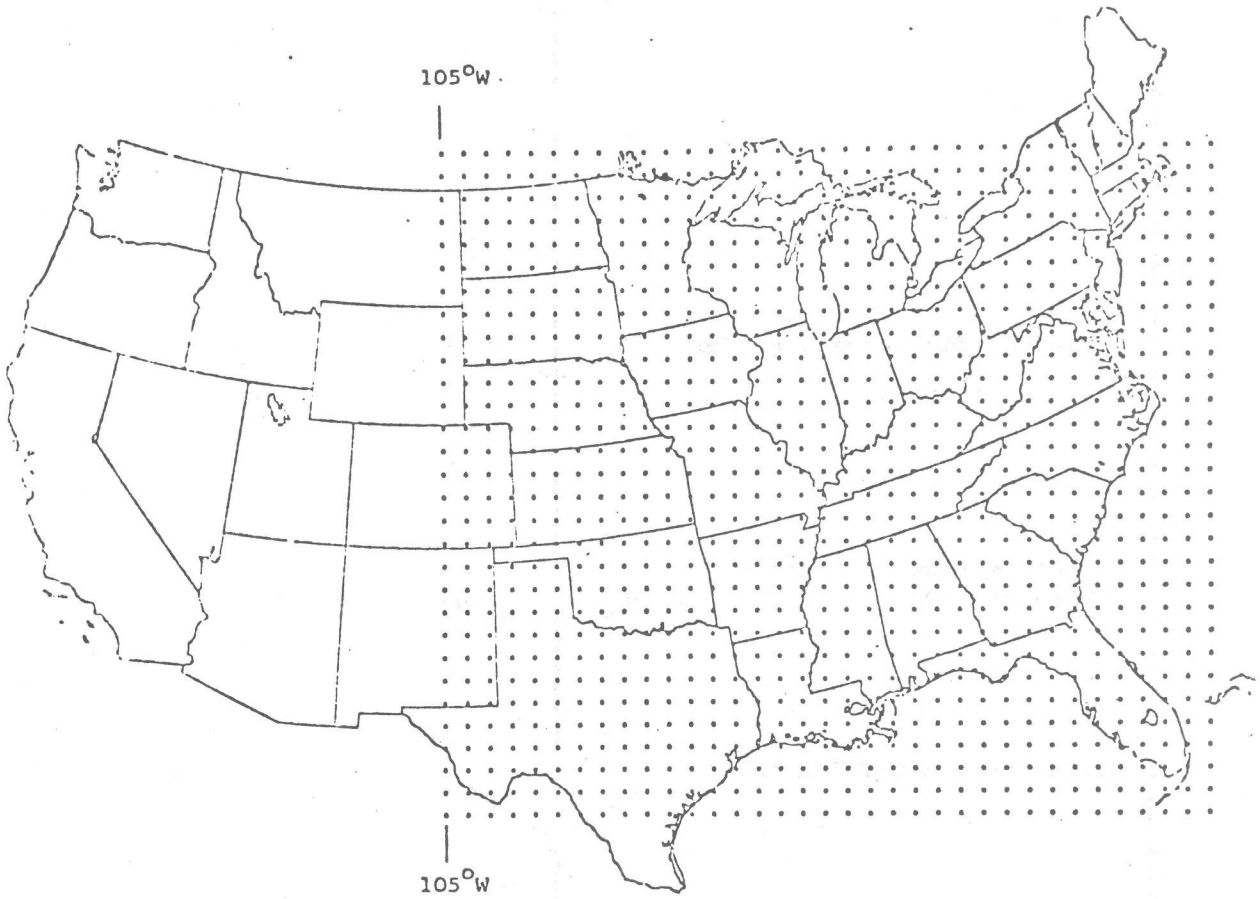

Figure 1.1.--Present forecast area covered by the boundary layer model. The average grid spacing over this area is 80 km.

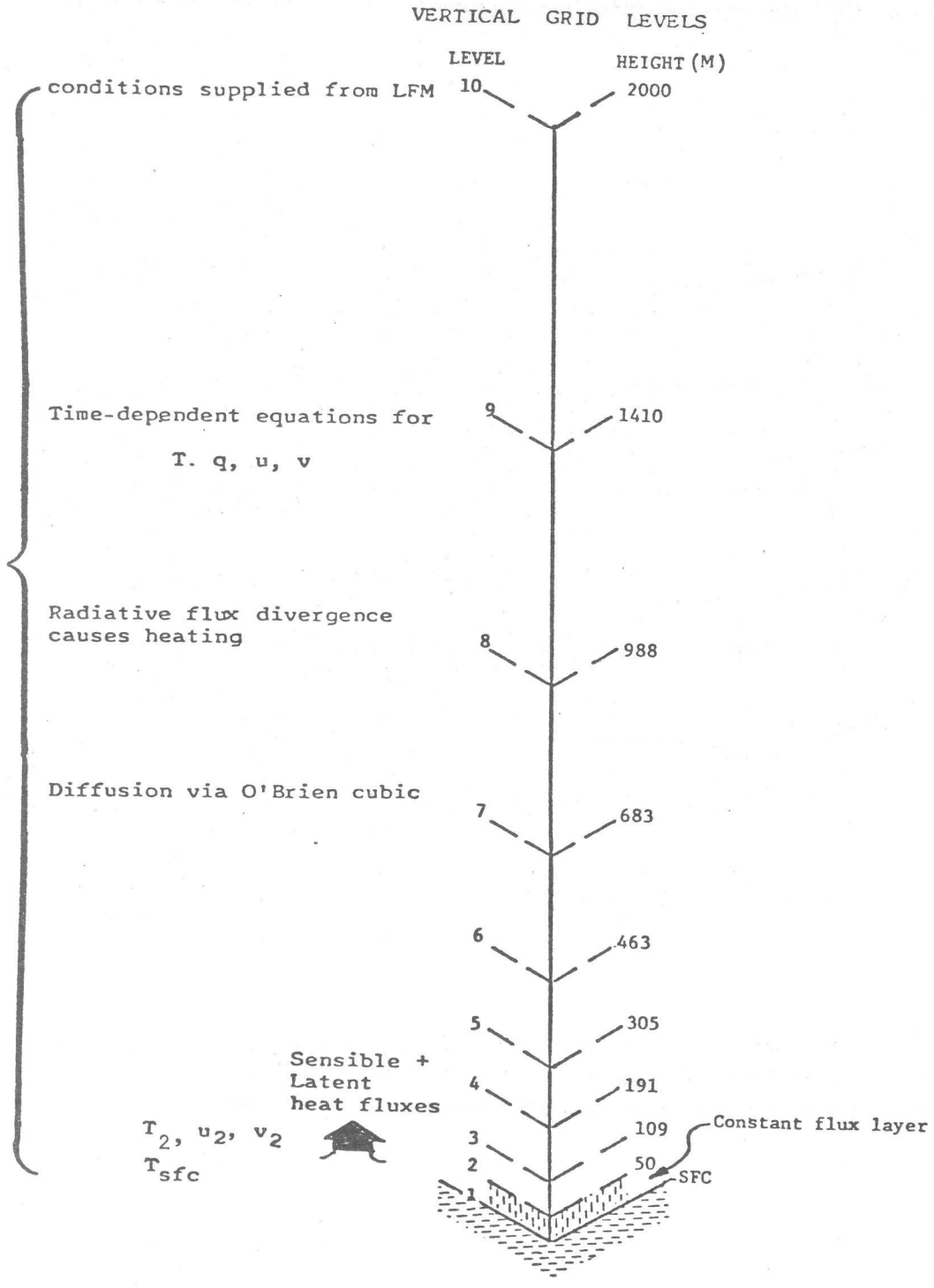

Figure 1.2.--Vertical structure of the boundary layer model.

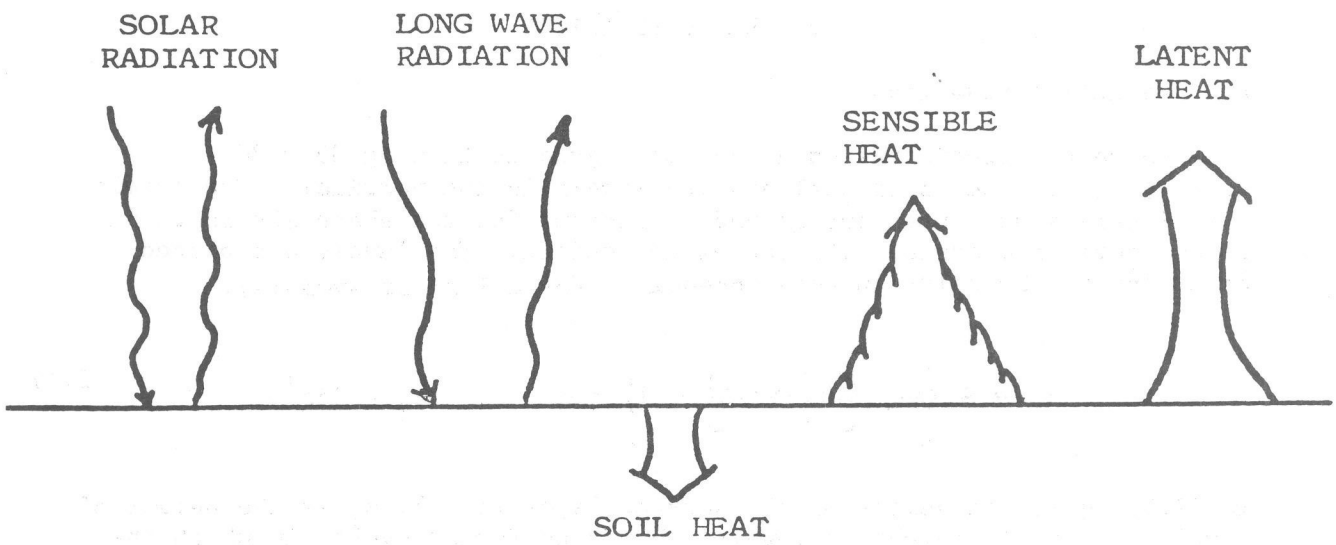

Figure 1.3.--The model solves an energy flux balance to obtain surface values for temperature and humidity.

to better define fields over water areas. There is an option to include the surface land stations which provide well-detailed surface fields. The analysis itself uses a successive approximation approach with the optimum influence radius of Stephens and Stitt (1970).

The model has shortcomings. One of these is the coarse horizontal mesh spacing of about 80 km, which for a bona-fide boundary layer model should be about 10 km. Nevertheless, the model encompasses 35 x 30 x 10 gridpoints (= 10,500 points) which provide for more horizontal resolution than that inherent in the synoptic data available for running the model. Furthermore, a greatly refined grid, excepting perhaps a telescoping grid of very limited area, is not now operationally feasible.

Another limitation is the use of K-theory. As is known from many numerical simulations in engineering, K-theory inadequately predicts many aspects of turbulent flow that are handled well by second moment and other more complex models. Models more detailed than K-theory models may, however, require much computer time. One of Deardorff's advanced boundary layer models (Deardorff, 1974) takes several days of computer time to make a 24-hour forecast. By contrast, TDL's K-theory model takes about eight minutes of CPU time. Of course, second- (or higher!) moment methods and a much refined grid could be conceivably added to the BLM. However, this would make the model much more difficult, if not impossible, to operate on a daily real-time basis.

2. BASIC RELATIONS

a. Predictive Equations

We solve the predictive equations on a grid containing 35 x 30 gridpoints in the horizontal and ten levels in the vertical. The levels are closely spaced near the ground to account for the sharp shears to be found there and expand with increasing height. The levels are placed according to the relation (see Appendix F for a list of symbols):

$$z_j = A\left\{\exp\left[(z_j'-h)/A\right] - 1\right\} + h \quad ; \quad z_j' = j\Delta z'. \tag{2.1}$$

In (2.1), h is the height of the surface layer (50 m), z_j is the height of level j and z_j' is height of level j in a transformed system in which the predictive equations are solved. The levels are spaced equally in the transformed system ($\Delta z'$ = constant = 50 m) as a matter of convenience. The transformed system requires the equations of motion to be recast wherever a derivative of z appears,

$$\frac{\partial}{\partial z} = \frac{dz'}{dz}\frac{\partial}{\partial z'} = g(z)\frac{\partial}{\partial z'}$$

$$g(z) \equiv \frac{dz'}{dz}. \tag{2.2}$$

The predictive relations for temperature, humidity, and wind use K-theory. The relations for potential temperature, Θ, and specific humidity, q, are

$$\frac{\partial\Theta}{\partial t} + \vec{V}\cdot\nabla\Theta = \frac{\partial}{\partial z}\left(K_T\frac{\partial\Theta}{\partial z}\right) + \text{radiative heating} \tag{2.3}$$

$$\frac{\partial q}{\partial t} + \vec{V}\cdot\nabla q = \frac{\partial}{\partial z}\left(K_T\frac{\partial q}{\partial z}\right), \tag{2.4}$$

in which $\vec{V}$ is the 3-dimensional wind vector.

We assume the K-coefficients for humidity and heat are equal and generally different from K_m, the transfer coefficient for momentum. The horizontal wind is predicted by,

$$\frac{\partial\tilde{W}}{\partial t} + \vec{V}\cdot\nabla\tilde{W} = \frac{\partial}{\partial z}\left(K_m\frac{\partial\tilde{W}}{\partial z}\right) - if(\tilde{W}-\tilde{G}). \tag{2.5}$$

In (2.5), $\tilde{W}$ and $\tilde{G}$ are complex horizontal and geostrophic wind vectors defined by,

$$\left.\begin{aligned} \tilde{W} &= u + iv \\ \tilde{G} &= u_g + iv_g \\ i &= \sqrt{-1}\ . \end{aligned}\right\} \tag{2.6}$$

The complex geostrophic wind vector is calculated by a method discussed in Section 3. The use of complex arithmetic conveniently couples the predictive equations for u and v. The subroutines that solve the equations of motion use complex arithmetic; thus (2.3) and (2.4) are combined in a similar fashion,

$$\frac{\partial \tilde{T}}{\partial t} + \vec{V}\cdot\nabla\tilde{T} = \frac{\partial}{\partial z}\left(K_T \frac{\partial \tilde{T}}{\partial z}\right), \tag{2.7}$$

in which

$$\tilde{T} = \Theta + iq\ . \tag{2.8}$$

The lower boundary conditions come from the surface layer relations and are described in the next subsection. We derive upper boundary conditions from the LFM data available at six-hour intervals with interpolation between the six-hour intervals. Because the BLM's initial analysis need not correspond to the LFM's, we do not use $\tilde{W}$ and $\tilde{T}$ derived directly from the LFM data but rather LFM tendencies, $\frac{\partial \tilde{W}}{\partial t}$ and $\frac{\partial \tilde{T}}{\partial t}$. These are used to update the initial BLM analysis at z = 2 km and provide continuously changing boundary conditions. LFM data are available on 700- and 850-mb surfaces which must be interpolated spatially to provide tendencies at z = 2 km.

The vertical wind component is computed from the continuity equation augmented, as is the geostrophic wind, by terrain effects,

$$w(z) = -\int_0^z dz \left(\frac{\partial u}{\partial x} + \frac{\partial v}{\partial y}\right) + \text{terrain effects}. \tag{2.9}$$

The negative of the vertical advection of (say) $\tilde{T}$, that is, $-w\frac{\partial \tilde{T}}{\partial z}$, adds to the K-shear term, $\frac{\partial K}{\partial Z}\frac{\partial \tilde{T}}{\partial z}$, and may be particularly important at night when the derivative of K is generally small.

The predictive equations are solved over a 24-hour period using half-hour time steps. Large time steps are needed to keep the computer time low enough for the model to be run operationally, but they strain the numerical techniques and the surface energy balance. The prerequisite of computational efficiency has led to a careful study of finite difference and related techniques, and also to new methods for solving the surface layer and energy balance-surface temperature relations. These methods will be presented in Section 3d and Appendix C.

b. Surface Layer Relations

Our early experiments with numerical solutions of the predictive wind equations convinced us that solving the relations from approximately the roughness height, z_o, to the top of the model, H = 2 km, requires too many closely-spaced levels and is not practical for an operational model. We therefore chose to introduce a quasi-static surface layer of thickness, h, for $0 \leq z \leq 50$ m, and to solve the predictive relations only in the transition layer, 50 m $\leq z \leq$ H. The surface layer is assumed to satisfy the Obukhov relations (Obukhov, 1946):

$$\left.\begin{aligned} \frac{\partial \Theta}{\partial z} &= \frac{\Theta_*}{kz}\,\phi_T(z/L) \\ \frac{\partial q}{\partial z} &= \frac{q_*}{kz}\,\phi_q(z/L) \\ \frac{\partial u}{\partial z} &= \frac{u_*}{kz}\,\phi_m(z/L) \\ L &= u_*^2\bar{\Theta}/(kg\Theta_*)\,. \end{aligned}\right\} \qquad (2.10)$$

The "universal functions" ϕ_T, ϕ_q, and ϕ_m have been approximated by Webb (1970) and Businger, et al. (1971) by:

$$\left.\begin{aligned} &\underline{L < 0}: \\ &\phi_T = \phi_q = .74(1 - 9z/L)^{-1/2} \\ &\phi_m = (1 - 15z/L)^{-1/4} \\ &\underline{L > 0,\ L \geq z}: \\ &\phi_T = \phi_q = .74 + 4.7\ z/L \\ &\phi_m = 1 + 4.7\ z/L \end{aligned}\right\} \qquad (2.11)$$

$$
\left.
\begin{aligned}
& z_o \leq L \leq z \\
& \phi_T = \phi_q = \phi_T \Big|_{z = L} \\
& \phi_m = \phi_m \Big|_{z = L} .
\end{aligned}
\right\}
\qquad \text{(2.11 cont'd)}
$$

Let us assume the wind is zero at $z = z_o$, and $\Delta\Theta \equiv \Theta(z=h) - \Theta(z_o)$ and $\Delta U \equiv U(z=h) - U(z_o)$ are known from the predictive and energy balance equations. Then by integrating the Obukhov relations

$$
\left.
\begin{aligned}
\Delta\Theta &= \frac{\Theta_*}{k} F \equiv \frac{\Theta_*}{k} \int_{z_o}^{z} \frac{dz}{z} \phi_T \, (z/L) \\
\Delta U &= \frac{u_*}{k} G = \frac{u_*}{k} \int_{z_o}^{z} \frac{dz}{z} \phi_m \, (z/L),
\end{aligned}
\right\}
\qquad (2.12)
$$

solving for u_* and Θ_* and substituting into (2.10), we can deduce a relation in which the only unknown is the Obukhov length,

$$
L = \frac{F(L)}{G^2(L)} S \quad \text{in which} \quad S \equiv \frac{\bar{\Theta} \Delta U^2}{g \Delta\Theta} . \qquad (2.13)
$$

Relation (2.13) can be solved exactly for the mildly stable case (defined as $L > 0$, $L \geq h$) but must be solved iteratively for the strongly stable (defined as $L > 0$, $L < h$) and unstable ($L < 0$) cases (Long and Shaffer, 1973),

$$
L^{(n+1)} = \frac{F\left[L^{(n)}\right]}{G^2\left[L^{(n)}\right]} S . \qquad (2.14)
$$

In (2.14), $L^{(n)}$ is the nth iterate; the first iterate is the nearly-neutral value of L. Convergence follows rapidly and requires only a few iterations. Exact analytical expressions for F and G are given in Appendix E. Once L has been calculated, Θ_* and u_* follow directly from (2.12).

The diffusion coefficients and their derivatives in the surface layer are computed from the following relations:

$$\left.\begin{aligned} K_T &= \frac{ku_* z}{\phi_T} \\ K_m &= \frac{ku_* z}{\phi_m} \end{aligned}\right\} \qquad (2.15)$$

The derivatives of temperature, humidity, and wind come from the Obukhov relations evaluated at z = h.

c. K-Profiles

Although K-theory is inadequate for predicting the details of the evolution of the boundary layer, more realistic closure techniques are beyond the reach of our operational model. Thus, we use K-theory as the vehicle for turbulent transfer in the transition layer.

Our numerical experiments show that a K dependent upon local stability is prone to induce subtle instabilities in the numerics of an otherwise numerically stable model. The small disturbances can grow and eventually swamp the model unless they are ruthlessly suppressed. There is a discussion on noise abatement in Section 2d.

A Hermite interpolation applied to a simple cubic, as suggested by O'Brien (1970), is a safe alternative. Because K and its derivative are given by the surface layer relations and K and dK/dz may be assumed small at the top of the model, O'Brien proposed that K(z) be approximated by

$$K(h \leq z \leq H) = K_h + \left(\frac{z - H}{H - h}\right)^2 \left\{ K_h - K_H + (z - h)\left[\left(\frac{\partial K}{\partial z}\right)_h + \frac{2(K_h - K_H)}{H - h}\right]\right\} \qquad (2.16)$$

The O'Brien K profile always assumes its largest value at z = (H-h)/3, regardless of the magnitude of K at the top and bottom points. It is more reasonable to allow the top of cubic profile to rise and fall with the mixed depth. We use a rate equation suggested by Deardorff (1971) when $\Theta_* \leq 0$,

$$\frac{1}{h_d}\frac{\partial h_d}{\partial t} = -c_p u_* \Theta_* / (\partial\Theta/\partial z)_+ + \text{advective effects}, \qquad (2.17)$$

in which h_d is the mixed depth height and $(\partial\Theta/\partial z)_+$ is the lapse rate above the mixed depth. At night, h_d is arbitrarily set to 350 m. The K's are set to a fixed value (0.5 m^2/s) above h_d. We have also examined nocturnal rate equations proposed by both Tennekes (1973) and Deardorff (1974) and find similar results.

d. Numerical Methods

The model cannot be run operationally unless its CPU time is kept very low. Efficiency requires the time step (Δt) in the integration of the predictive equations to be large. Research boundary layer models typically use Δt from several seconds to a few minutes. On the other hand, we are able to use half-hour time steps because: (1) the surface temperature calculation treats the soil heat flux analytically rather than with a finite difference expression (Shaffer, 1978), (2) surface layer relations are used in place of predictive equations below 50 m, (3) the equations for vertical diffusion are solved with highly stable implicit schemes that strongly damp unrealistic short waves, and (4) the horizontal advection equations are solved with an implicit chapeau function relation which is linearly stable for unlimited time steps.

Because the vertical diffusion and horizontal advection schemes are implicit and require solving systems of simultaneous equations, we use the splitting method (Yanenko, 1971). Integration from time t to $t + \Delta t$ involves first solving the vertical transfer and advection equations implicitly, followed by the X-advection and finally the Y-advection.

The heat and moisture vertical transfer equation is

$$\frac{\partial \tilde{T}}{\partial t} = g \frac{\partial}{\partial z'} \left(K_T g \frac{\partial \tilde{T}}{\partial z'} \right) , \qquad (2.18)$$

when expressed in terms of the z' coordinate system. The popular Crank-Nicolson scheme replaces the time derivative by a forward difference and averages (equally) the spatial derivative at time t and $t + \Delta t$. This leads to an implicit, tridiagonal system of equations which can be solved easily with a double sweep procedure. Although Long (1973) shows the Crank-Nicolson method is generally superior to most other simple schemes, it may fail when K depends upon local stability. The probable reason for the failure and curative measures are discussed in Long (1978b). Two solutions are proposed. One involves a 4th-order scheme that damps $2\Delta z$ waves heavily; the other is a 2nd-order scheme that removes $2\Delta z$ waves completely at each time step. Both methods have been tested and seem highly stable. The level spacing is arbitrary for both schemes; a $z \rightarrow z'$ transformation is not needed. The BLM currently uses a scheme similar to the two new schemes except a hypothetical z' system is required. In the near future, we will convert to the scheme that removes $2\Delta z$ waves. We note for completeness that our tests show that linear finite elements do not seem to offer any particular stability advantage over the above schemes, and are as prone to unrealistic oscillations as the Crank-Nicolson finite difference scheme. Appendix D lists expressions for the finite element, 4th-order, and damping schemes.

The horizontal advective portion of the predictive equations are accurately solved by using linear chapeau functions. The virtues and deficiencies of chapeau functions, as well as the details of their application, can be found in Long and Hicks (1975) and Long and Pepper (1976). One useful property is their low reflectivity at outflow boundary points. However, large negative group velocities can reduce the accuracy of chapeau functions in regions of large mesh length increases and strong local forcing. We are now investigating generalized chapeau methods. Relations for the chapeau function solution of the advection equation are given in Appendix D.

One particularly distressing shortcoming of the model is the strong local forcing sometimes created by vertical turbulent transfer. The local forcing "shocks" the horizontal advection equations at each gridpoint and produces heavy shortwave noise. Horizontal filtering of the u_* and Θ_* fields reduces the noise considerably. We have devised a useful implicit filter which can damp two-grid interval noise while leaving longer waves untouched. If Q_j and $\overline{Q}_j$ are the unsmoothed and smoothed values of Q at gridpoint j, then the implicit filter is given by

$$A_j \overline{Q}_{j-1} + B_j \overline{Q}_j + C_j \overline{Q}_{j+1} = D_j \tag{2.19}$$

where

$$\left.\begin{aligned} A_j &= C_j = 1 - \delta \\ B_j &= 2(1 + \delta) \\ D_j &= 2Q_j + Q_{j-1} + Q_{j+1} \end{aligned}\right\} \tag{2.20}$$

and $\delta \to 0^+$. If $\delta = 0$, the filtered and unfiltered values are equal. Setting $\delta \to 0^+$ causes the two-grid waves to be completely removed while longer waves are undamped. When δ is increased to $\delta = 1$, the filter reduces to a standard smoother. Our experiments show that most of our noise problems are eliminated by careful use of the implicit filter.

3. SURFACE AND PHYSICAL EFFECTS

The upper-air data which are used for the model's initialization have an average separation of approximately 400 km. By assuming that the minimum resolvable wavelength in the data is twice this distance, or 800 km, this represents a $10\Delta x$ wave on our grid. If the initial data can resolve only an 800 km wave, the final forecast can be expected to have the same general

scale unless smaller-scale features can be introduced. The most likely place to incorporate smaller-scale features is at the surface. Here we encounter changes of elevation, surface vegetation, albedo, and soil thermal and moisture properties. By introducing these features on scales smaller than that of the initial upper-air data, we may be able to produce some mesoscale features which will have a pronounced effect upon the final forecast.

a. Model Terrain

The model's terrain was derived from the average elevation for each 1° latitude by 1° longitude box. This scale is comparable to our computational grid. The elevation data were analyzed to yield elevations at each BLM gridpoint (see Section 4 for the methods used). A two-dimensional representation of the terrain appears in figure 3.1.

b. Surface Roughness, z_o

Since the surface layer formulation involves the surface roughness, z_o, fluxes of heat and momentum will be affected by the horizontal variations in z_o. In order to obtain values of z_o over our grid, we first assume that z_o is a function of vegetative cover only. (More precisely, we expect undulations in the surface topography to contribute to z_o. This will be investigated later.) To establish general vegetation cover over our grid, we first determine the principal land use type, in each ½° latitude by ½° longitude box, from a map of "Major Land Uses in the United States" (U.S. Department of Agriculture, 1958). Land use includes categories such as metropolitan cities, ungrazed forest, cropland, and pasture land. We assign to each category a value of z_o which ranges from 1 m over forested areas to 1 cm over pastured areas. These values of z_o are then analyzed giving the map of z_o shown in figure 3.2.

c. Soil Thermal Properties

Maps of soil thermal diffusivity and conductivity were similarly established starting with a map of soil types throughout the United States (U.S. Department of Interior, 1967). Representative thermal properties were assigned to each soil type.

d. Surface Energy Balance and Radiation Effects

Each of these surface characteristics, discussed above, influences the model through the surface energy balance from which the surface temperature and humidity are computed. At the surface, we are concerned with the fluxes of sensible heat, latent heat, soil heat, longwave radiation, and shortwave radiation (fig. 3.3). The sensible and latent heat fluxes can be expressed as

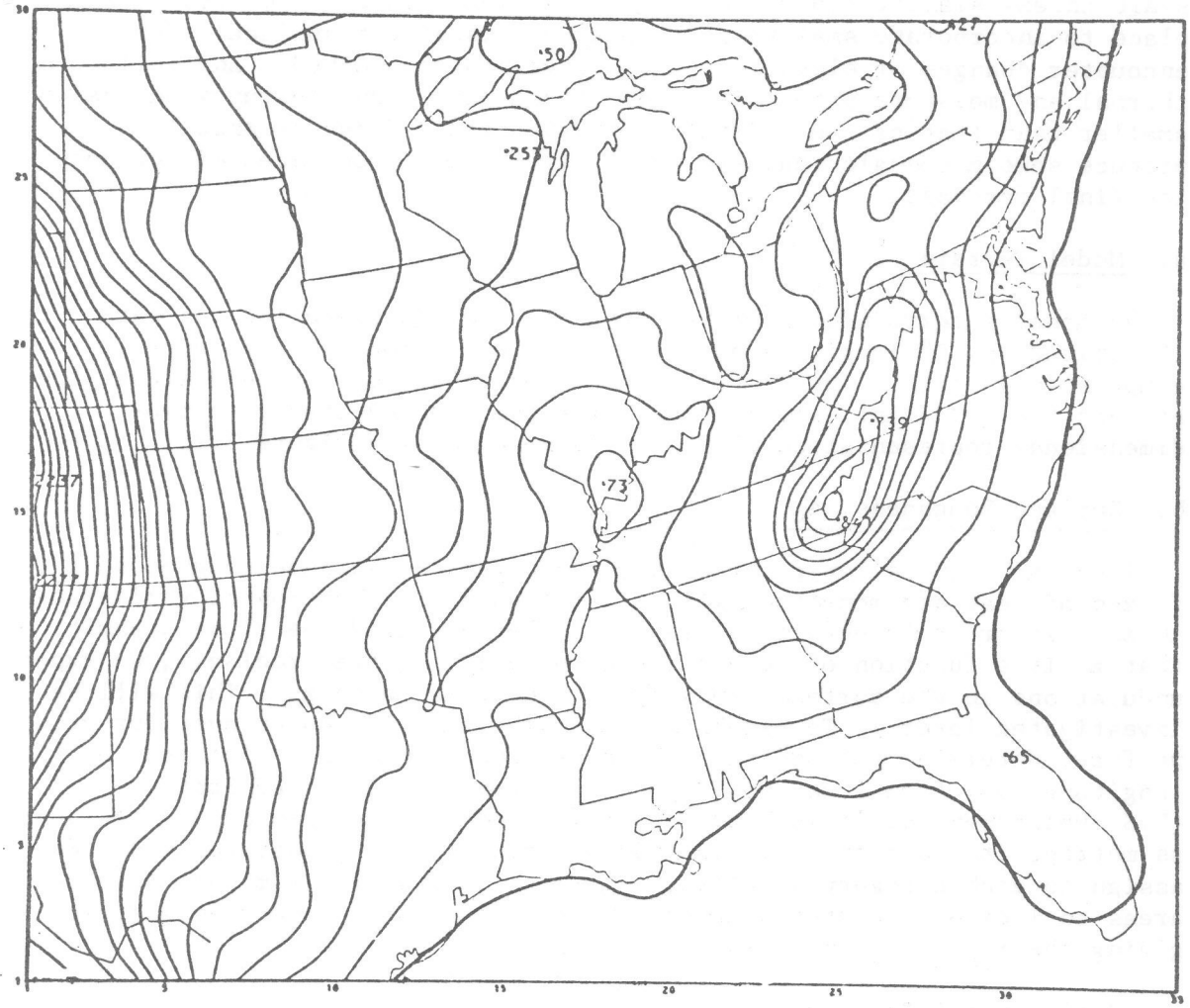

Figure 3.1.--The model's terrain contoured at intervals of 100 m. The map is based on the average elevation in a 1^{o} latitude by 1^{o} longitude box, analyzed to give values at each BLM gridpoint.

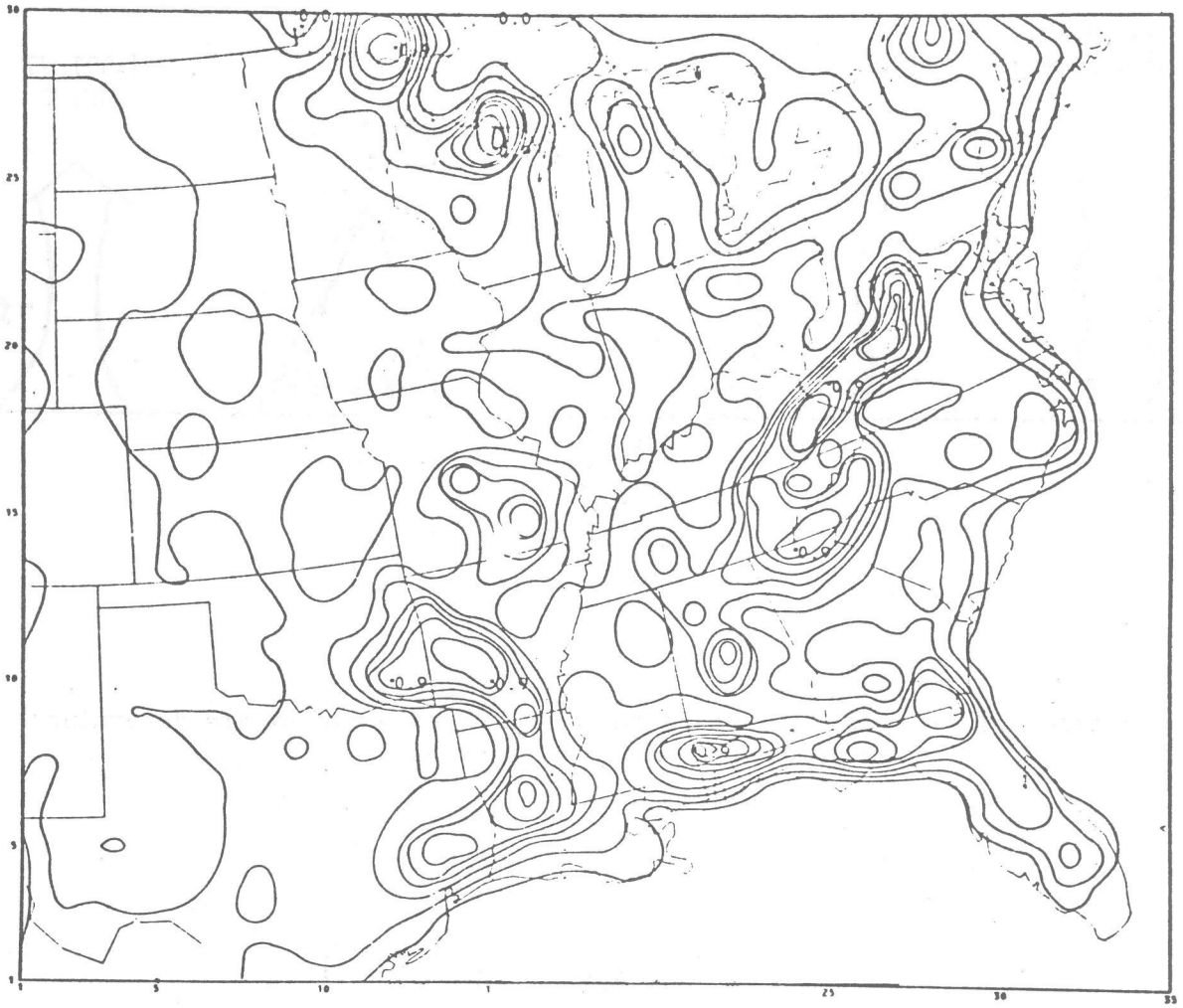

Figure 3.2.--Surface roughness, z_o, used in the BLM is contoured at 0.1 m intervals. Values of z_o are determined from the land use in boxes $\frac{1}{2}^o$ latitude by $\frac{1}{2}^o$ longitude. Large values of z_o represent forested areas; small values are given to areas with only short vegetation. The influence of subgrid scale terrain variation on z_o is not considered.

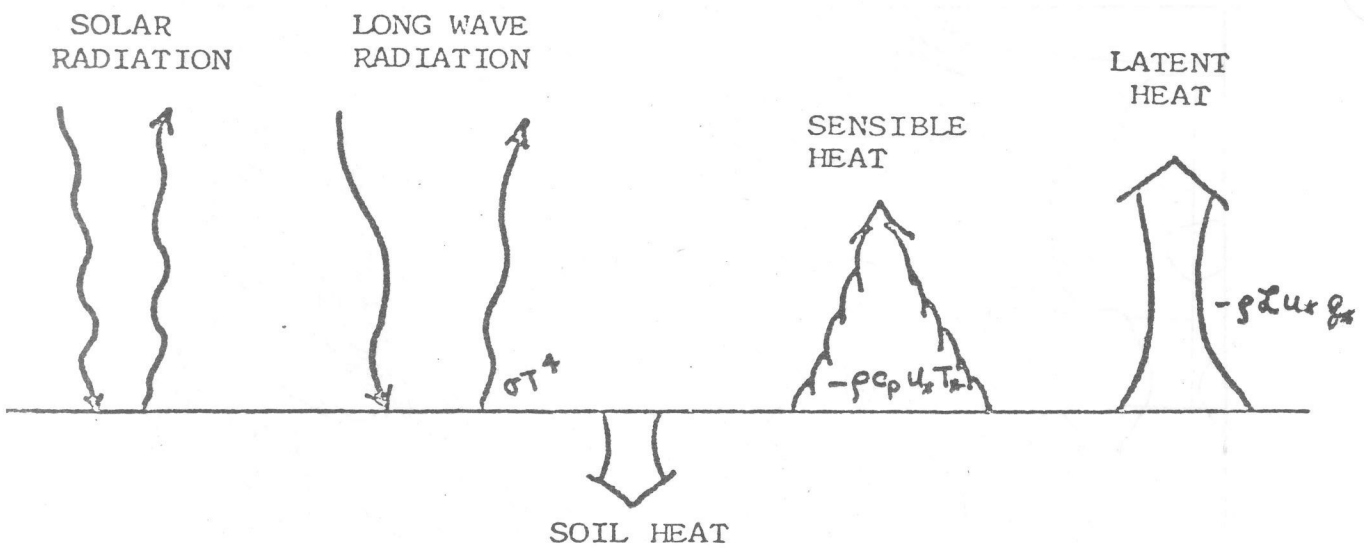

Figure 3.3.--The BLM's surface temperature and humidity are determined through surface energy flux balance.

$$\left.\begin{aligned} F_{\text{sensible}} &= -\rho c_p u_* \theta_* \\ \text{and } F_{\text{latent}} &= -\rho \mathcal{L} u_* q_* , \end{aligned}\right\} \tag{3.1}$$

where c_p is the specific heat of air at constant pressure, ρ the density of air, and $\mathcal{L}$ the latent heat of evaporation. From (2.10) it follows that q_* is related to θ_* through the relationship

$$q_* = \theta_* \left(\frac{q_h - q_{sfc}}{\theta_h - \theta_{sfc}} \right) . \tag{3.2}$$

Here h is the top of the contact layer (50 m). An assumption must be made to evaluate the surface humidity. We assume that the ratio of actual evaporation to potential evaporation remains constant throughout the forecast period (Halstead, et al., 1957),

$$H = \frac{E_{actual}}{E_{potential}} \triangleq \frac{q_h - q_{sfc}}{q_h - q_{sfc}\ (\text{saturated})}. \qquad (3.3)$$

The surface specific humidity is readily computed after a value of H is prescribed and the value of q_{sfc} (saturated) is computed through Tetens equation (Gerrity, 1967).

Radiation drives the diurnal changes in temperature. Our long-wave radiation calculation, shown in detail in Appendix A which is reproduced from Shaffer and Long (1973), closely follows the treatments of Atwater (1970) and Pandolfo, et al. (1971). Basically, both water vapor and carbon dioxide are considered as emitters of long-wave radiation. Clouds play an important role and act as "black bodies" for long-wave radiation.

Short-wave radiation is partially depleted as it passes through a clear atmosphere to the surface. Water vapor and other atmospheric absorbers are responsible for part of this, along with scattering by dust particles and molecules. Appendix B, reproduced from Shaffer and Long (1973), gives the details of the short-wave radiation calculation.

Clouds, of course, cause the greatest variation in the short-wave flux reaching the surface. Ideally, clouds should be specified in several layers to compute the surface radiation. Each layer would be assigned a transmission coefficient and the appropriate surface flux could be computed with reasonable accuracy. However, forecasts of a general fractional cloud cover are inaccurate.

Our first, and preferred, source for a cloud forecast is the LFM model. Unfortunately, its cloud forecasts are of little value for the layers above the boundary layer. Within a given layer, the LFM assumes total cloud cover if its relative humidity exceeds a prescribed value, and no clouds if the relative humidity is below this figure. The other available source of cloud forecasts is the Model Output Statistics (MOS) forecasts. These are available for 164 stations within our grid at 6-h intervals after the usual data collection times of 0000 GMT and 1200 GMT. The MOS forecasts give probabilities for the categories of clear, scattered, broken and overcast. We assign the most likely category to that station, then assign a fractional sky cover value for each of the four categories. After this is completed for every MOS station, the fractional sky cover field is analyzed. The analysis assigns a cloud amount to each gridpoint. The cloud amount is calculated for each of the 6-, 12-, 18- and 24-h forecasts. The initial cloud field is based on the analysis of the observed cloud amounts. Continuous cloud amounts follow from linear interpolation in time.

In addition to computing surface radiation fluxes, we also calculate the heating within each layer due to flux divergences. The temperature change from flux divergence has a very beneficial effect. During the

convective portion of the day, temperatures rise at all levels within the mixed layer. At night, diffusion is extremely small. Without the cooling from flux divergence, the temperature remains at about the value it reached during the unstable hours, creating a net warming trend. When the cooling from radiative flux divergence is added, nocturnal temperatures decrease, giving approximately the same temperatures from one dawn to the next. Figure 3.4 demonstrates the effects of radiative flux divergence in a one-dimensional model's simulation of Wangara data.

There remains the problem of calculating soil heat flux for the surface energy balance. Again, the details are deferred to Appendix C which is reproduced from Shaffer and Long (1973). The method uses an analytic solution of the heat equation and assumes that: (1) the soil thermal coefficients are constant, and (2) the initial soil temperature is known. The soil heat flux reduces to

$$C\,T_{sfc} + C' , \tag{3.4}$$

where C and C' depend upon the initial soil temperature profile, the soil's thermal properties, and the previous soil heat fluxes.

Inserting each of these fluxes into an energy balance equation, we get

$$\mathcal{E} = 0 = \rho c_p u_* \Theta_* + \rho \mathcal{L} u_* q_* - (C\,T_{sfc} + C') - \varepsilon_s \sigma T_{sfc}^4 + R_{net} . \tag{3.5}$$

Here $\varepsilon_s \sigma T_{sfc}^4$ is the long-wave flux from a surface of emmissivity ε_s. R_{net} includes all short-wave and long-wave fluxes at the surface except $\varepsilon_s \sigma T_{sfc}^4$.

Since u_*, Θ_*, and q_* are all functions of the surface temperature and the surface emission varies as T_{sfc}^4, the energy equation is highly nonlinear. A Newton-Raphson iteration technique is used to solve for temperature

$$T_{new} = T_{old} - \frac{\mathcal{E}(T_{old})}{\left(\frac{\partial \mathcal{E}}{\partial T}\right)_{T_{old}}} . \tag{3.6}$$

Although each iteration requires a new surface layer calculation of u_* and Θ_*, the scheme is efficient and works well even for long (half-hour) time steps. In general, only two or three iterations are required for convergence which requires

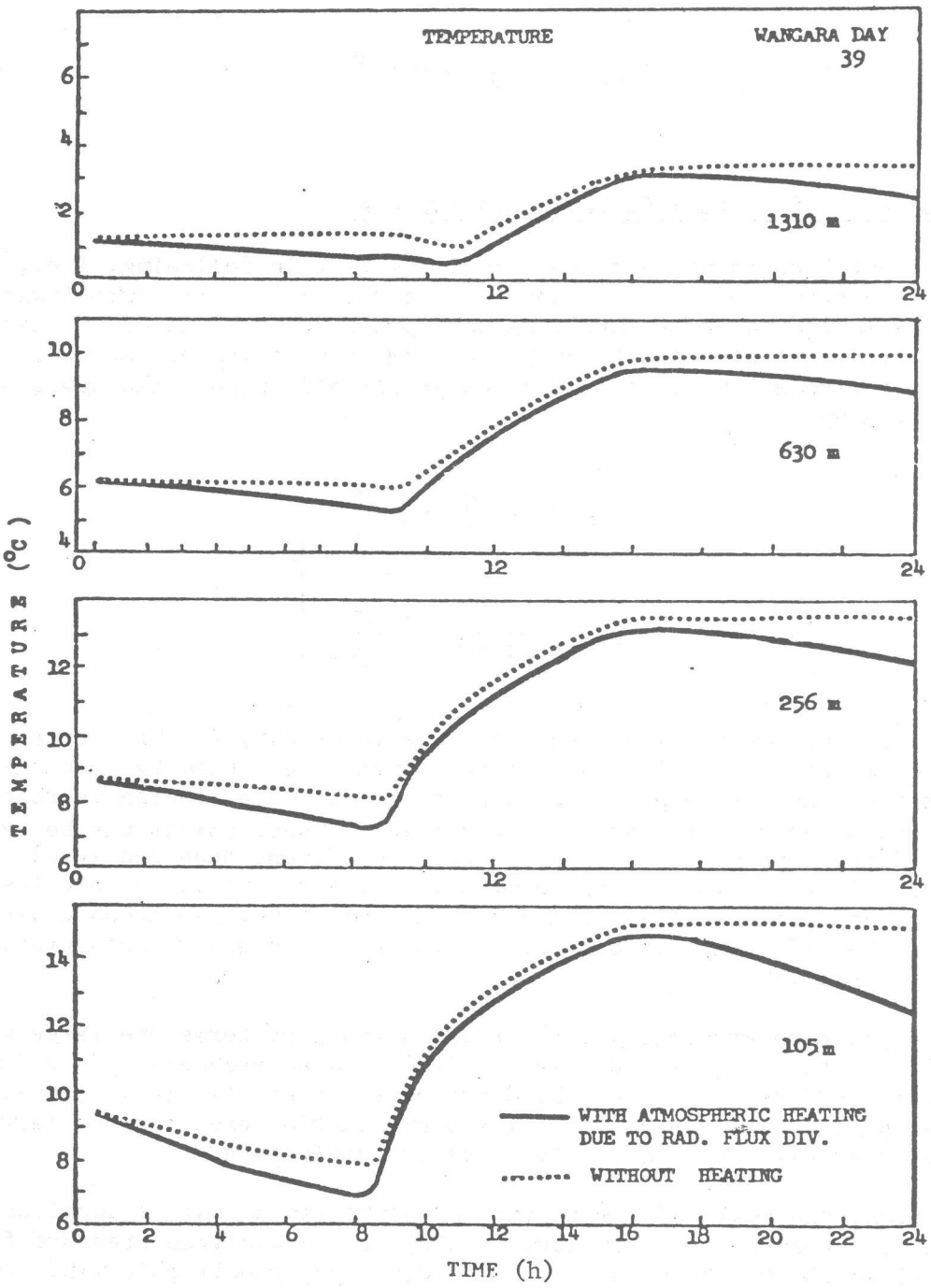

Figure 3.4.--Results of running the one-dimensional model with and without radiative heating due to flux divergence.

$$|T_{new} - T_{old}| \leq 0.05^{o}C \ . \qquad (3.7)$$

e. The Effects of Terrain-Following Coordinates

The horizontal coordinates of the model are terrain following, i.e., each level is a constant height above the model's terrain. Terrain-following coordinates introduce terms involving horizontal derivatives of the terrain into the horizontal wind equations. The terms can be lumped together with the pressure gradient term to form a new geostrophic wind. The new geostrophic wind is given by

$$\left.\begin{aligned} u_g &= -\frac{1}{\rho f}\frac{\partial p}{\partial y} - \frac{g}{f}\frac{\partial E}{\partial y} \\ v_g &= \frac{1}{\rho f}\frac{\partial p}{\partial x} + \frac{g}{f}\frac{\partial E}{\partial x} \ . \end{aligned}\right\} \qquad (3.8)$$

The height of the terrain above sea level is denoted by E. The terrain gradient term compensates for the change of pressure caused by a change in the elevation. Let us suppose two separate points on a sloping terrain are at different heights above the earth's surface. These points may be expected to have different pressures because of their different mean sea level elevations. If there is no horizontal pressure gradient in coordinates of constant height above sea level, there should be no net geostrophic wind because of the difference in elevation. The pressure and terrain gradient terms should cancel.

Both the pressure gradient and the terrain gradient terms are large when the model's terrain changes sharply. This can cause problems. In order to reduce errors created by taking the difference between two large terms, the terms must be evaluated carefully. The approximation used for the terrain derivative must also be used for the pressure derivative.

In addition, the scale of the initial pressure field must be identical to that of the terrain. If we naively introduce an analyzed pressure field and an arbitrarily rough terrain into the equation, geostrophic winds on the order of 10^3 m/sec are likely to result! In order to assure that our model's terrain and pressure field match, we first analyze the pressure field, then derive an analyzed terrain field based on the elevations of those stations used for the pressure analysis. If a pressure observation is not reported or is eliminated due to errors, the corresponding station elevation is not used. The terrain field is filtered in a manner identical to that of the pressure field.

We find that the elevation field must be recomputed for each model run. We once accidentally included an elevation measurement without the corresponding pressure observation. The result was a large error in the geostrophic wind field.

Since the analysis terrain is based on only about 50 measurements over our grid area, the terrain is extremely smooth. To operate the model on a rougher, more realistic terrain, we must convert the pressures from the smooth analysis terrain to the desired model terrain. In some areas of our grid, these two terrains differ by over 500 m. A lapse rate for temperature must be assumed in order to change the pressures from one level to another. We use the standard atmosphere lapse rate near the surface, -6.5°C/km. (Other lapse rates were also tried--adiabatic, and other non-standard atmospheres. Results were very similar.) The pressure is recomputed hydrostatically at the new model elevation.

When the geostrophic wind was recomputed from the model terrain with the new adjusted pressures and compared to geostrophic winds computed with the original analyzed pressures and the analyzed terrain, the differences in geostrophic winds were less than 0.5 m/sec. Sample calculations show that our method is consistent and does not add spurious error to the model.

Terrain-following coordinates require that extra terms be added to the relation for vertical velocity. The integrated form of the continuity equation,

$$w_h = \int_{\xi=0}^{h} \left(\frac{\partial u}{\partial x} + \frac{\partial v}{\partial y} \right) d\xi \,, \tag{3.9}$$

must be augmented by $\vec{V} \cdot \nabla E$. Thus, we have

$$w_z = w_h + \left(u \frac{\partial E}{\partial x} + v \frac{\partial E}{\partial y} \right) . \tag{3.10}$$

4. PREPARATION AND OBJECTIVE ANALYSIS OF INITIAL DATA

a. General

Our main objective is to retrieve available observations from the National Meteorological Center's (NMC's) data files, build significant and mandatory level soundings which are free of gross errors, and map the soundings to the boundary layer grid. The largest obstacles have been finding and overcoming errors in the data. It follows that the larger part of the initial data program is devoted to this problem.

Most of the processing and error detection program is specifically designed for the TDL BLM and is unique. The objective analysis algorithm, however, is based on the well known and widely used successive corrections procedure. There have been important features developed for our objective analysis which make it different from most other applications. We select the "best" influence radius which also determines the response of the low pass filters used in the analysis.

Additional processing is required at the end of the analysis step. We construct a marine profile of temperature over the water areas. We also prepare cloudiness estimates for the entire forecast period.

b. Data Processing and Error Checking

We select and store all the land, marine, and aircraft observations within five grid lengths of the lateral boundaries ($\Delta x = \Delta y \sim 80$ km). We typically receive 50 upper air, 25 ship and buoy, and 500 land reports. Aircraft reports with information in the lowest 2 km of the atmosphere are rare and are not a consistent source of information. Figures 4.1 and 4.2 show the distribution of the reports. We find about 10 levels of wind information to define the boundary layer wind profile up to 2 km.

The significant and mandatory levels of the upper air reports give detailed profiles of temperature and dewpoint as functions of pressure, and winds as functions of height, z. We interpolate temperature and dewpoint to each model z level using the log of the pressure as our vertical "coordinate." We must know the geopotential-pressure relationship which is not directly given in the reports for each sounding. We build the pressure-height profile hydrostatically. Our choice of vertical coordinates (log of pressure) is consistent with this relation.

We find it necessary to check the surface parameters carefully because these form the critical reference values for the vertical interpolation. Fortunately, there is an abundance of surface data upon which we can base a statistical checking system. We check surface (2 m) temperature, dewpoint, and station pressure. The station pressure is the most critical field. This will form the base of our sounding profile and determine our spatially dependent geostrophic wind estimate. The pressure is reported to the nearest integer millibar. This is crude for our needs, but is consistent with the accuracy ($\pm$ 0.5 mb) of pressure instruments [see Fankhauser (1974)].

All our statistical checking has the same form. For each observation, we search for other observations within a specified distance (2.25 grid units for a land observation and twice that for a ship). These choices are related to the average separation of the type of observations which is discussed later. For this sample of stations, we calculate the sample average, variance, and the 3rd moment about the mean (the skewness) if the variance meets certain criteria. When the variance gives inconclusive results, the skewness may be a useful parameter to detect data errors.

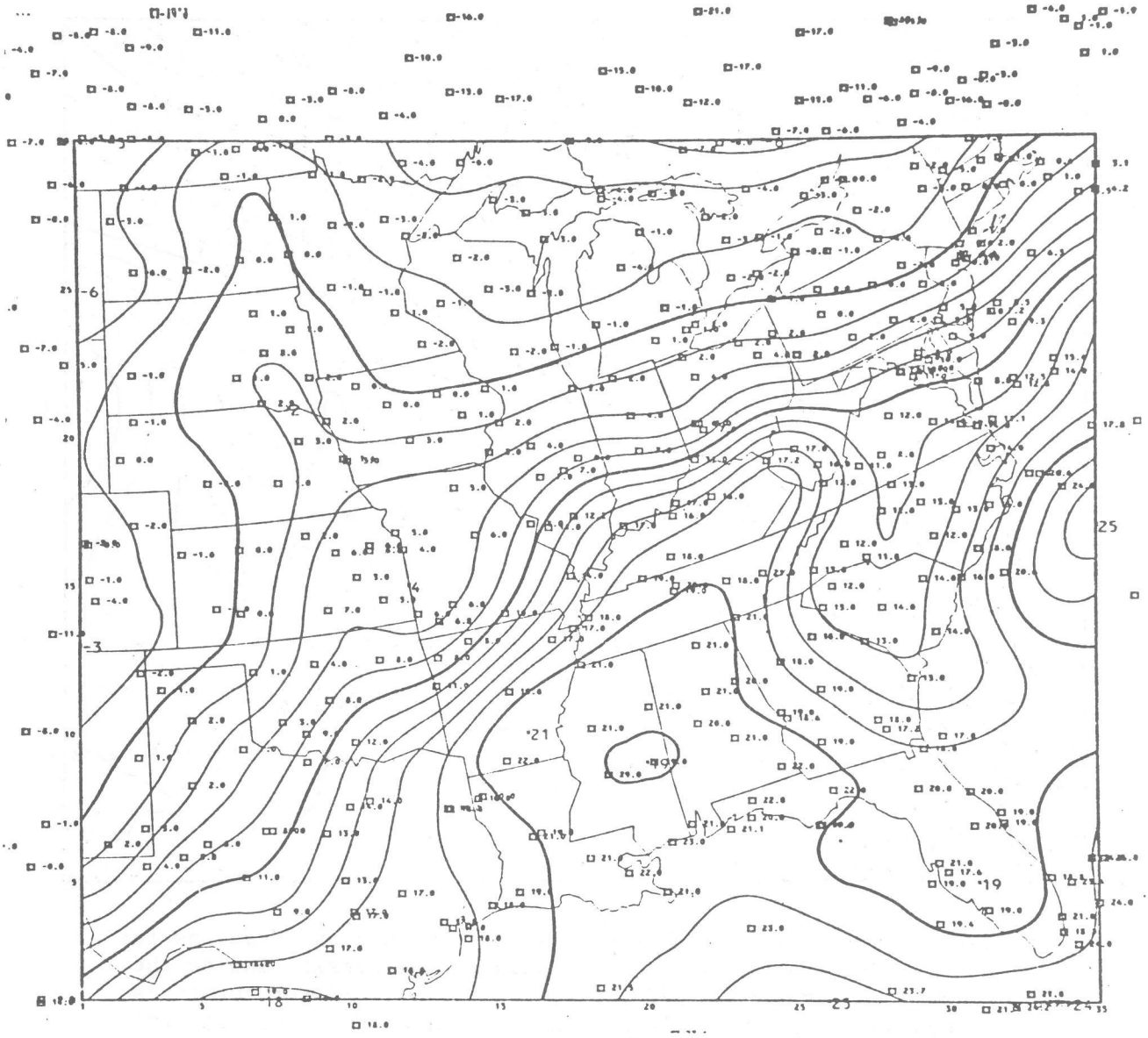

Figure 4.1.--Surface (2 m) temperature (^{o}C) analysis for 1200 GMT, March 18, 1977. Contour interval is 2 degrees with the 0, 10, and 20 degree isotherms emphasized. Small boxes are observation locations. Observations are listed to the right of each box. The analysis variance is 98.7 percent of the observation variance with an analysis root mean square error of 0.98 degrees. The 361 reports inside the grid have an average separation (D) of 1.7 grid units. The filter cutoff is set to integer (2D + .99) = 4 grid units.

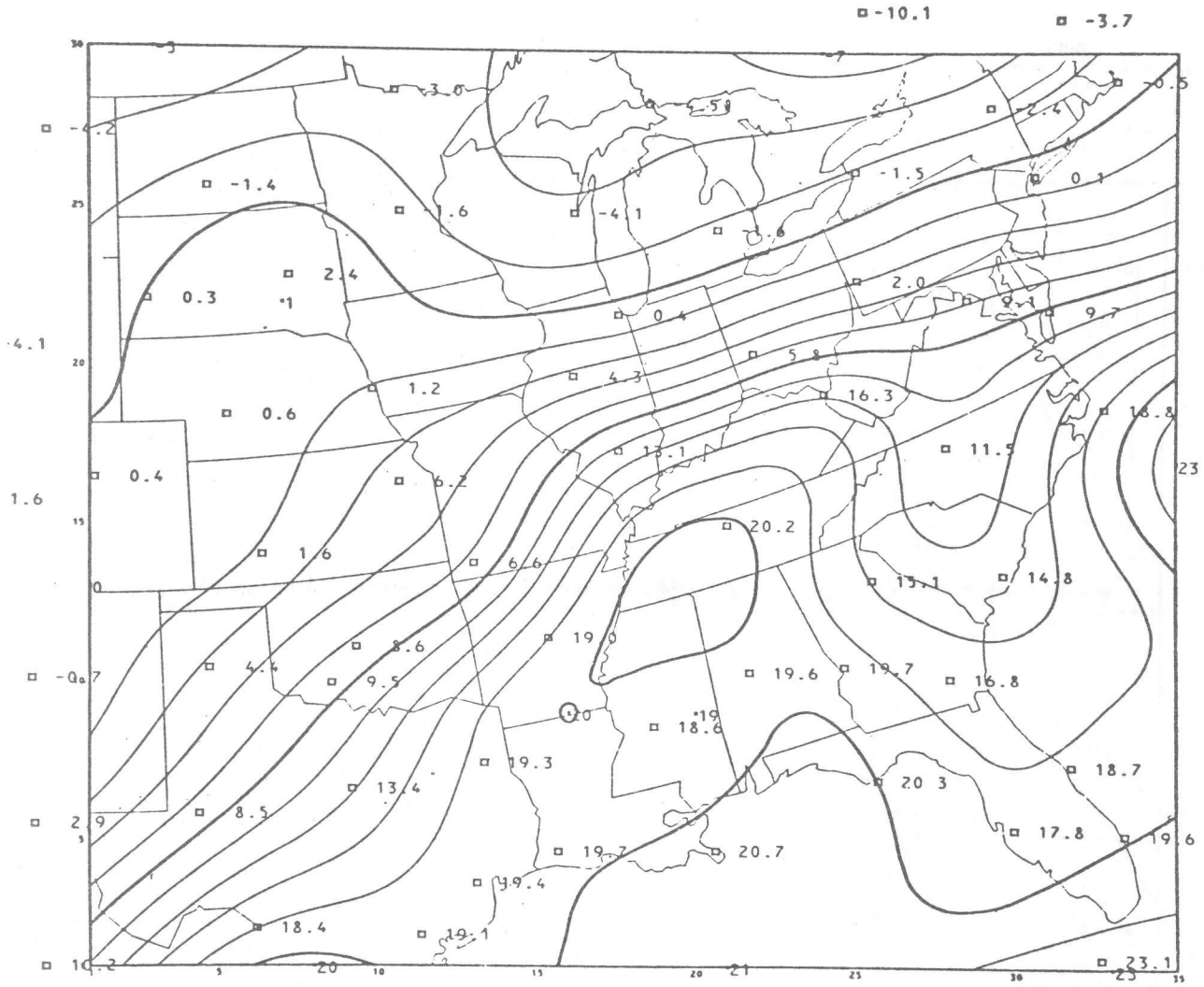

Figure 4.2.--50 m temperature (^{o}C) analysis contours and observations for 1200 GMT, March 18, 1977. Observational density inside the grid has dropped to 52 reports (D = 4.4). Filter cutoff is now set to 9 grid units. Analysis variance is 99.1 percent of the observation variance with a root mean square error of 0.82 degrees.

Error limits for the sample are based on these statistics. When reports are near coastlines, we make allowances for additional variance because of the rather large land-sea contrasts. Using the Cressman weight function defined as

$$\left.\begin{aligned} C_w &= \frac{D^2 - R^2}{D^2 + R^2} \qquad D > R \\ C_w &= 0 \qquad\qquad\quad D \leq R, \end{aligned}\right\} \tag{4.1}$$

where D is the maximum specified influence distance and R the distance to the observation from the center of the influence circle, we require that each report be within

$$\pm\ (2 - C_w)\,\sigma S(\sigma^2)F \tag{4.2}$$

of the sample average. Here, σ is the sample standard deviation and F is an empirical parameter which depends upon the variance. The limits imposed by equation (4.2) attempt to allow for meteorological variability and still detect gross errors. The extremes of the distance-dependent error limits are 0.8 and 4.6 standard deviations from the average.

Before checking the upper air surface pressures, we reduce them to sea-level to decrease elevation effects. Earlier versions of the reduction method applied the standard sea-level pressure reduction formula. This formula is a function of a station's 12-h mean temperature as well as other station-dependent parameters, like the plateau correction. When we applied a scheme for deducing the mean temperature for each upper air station from a collection of surrounding surface land stations, an occasional serious error was introduced into our calculations. The error didn't appear all the time because we used a collection of stations. However, when certain key stations were absent from the collection, the strong station dependence of the formula led to incorrect estimates for the sea-level pressure at the upper air stations.

We switched to the altimeter setting formula (Smithsonian Meteorological Tables, 1951) in which the only station dependent parameters are station elevation and station pressure. The pressure checking is now performed on reported altimeter settings from surface reports and our calculated upper air station altimeter settings. We find this method is relatively error free and reliable.

We don't rely entirely upon this one check for station pressure. The sea-level pressure field is also objectively analyzed and an analysis-observation deviation check is made for the upper air stations. This is very effective in catching errors greater than 1.5 mb, which are surprisingly common. We replace the reports violating our criterion with the analyzed value and adjust the pressures of the vertical levels to agree with the pressure correction at the surface.

One last check on the surface pressure field is made during the analysis of surface pressure. We compare our geostrophic wind estimates, interpolated to ship locations, against ship reported winds. Errors are probable if these two don't agree within 15 ms^{-1}. We assume the ship pressure is at fault, remove it from the observation list and then reanalyze the surface pressures.

Because of the importance of the surface parameters, we try to correct detected errors. We replace erroneous rawinsonde values with a Cressman weighted average of the sample observations when possible. This is not done very often, but seems to have positive effects.

We are now ready to build the geopotential-pressure profile and vertically interpolate to model levels. Vertical changes in temperature and moisture are checked for consistency. We try to eliminate unrealistic inversions and super-adiabatic lapse rates that occur over great depths or are related to temperature sensor evaporative cooling. We are able to detect sign errors in many cases.

Winds are linearly interpolated with height and are also checked for vertical and horizontal consistency. Only very crude wind checks can be performed. Horizontal statistical checks on the speeds are made and extreme changes in the vertical are eliminated (> 100 ms^{-1} from one level to the next).

After we divide the observations into two groups--inside or outside the grid--we are ready for the objective analysis.

c. Objective Analysis (Mapping)

We apply the widely used, simple, and effective procedure of successive corrections (Bergthorssen and Doos, 1955), with some important additions. The method is not formally optimal. It is fast, easily programmed, reliable and accurate. The essential ingredient that separates the successive corrections method from so-called optimal analysis procedures (Gandin, 1963) is the choice of weight function. The optimum methods incorporate correlation functions which are intended to model atmospheric structure. The weight function in the successive corrections method represents a similar attempt. There is considerable disagreement about the form of the correlation. Boundary layer relationships are even more unclear. In the absence of this information, we estimate the weight by using the isotropic function given by equation (4.1) where we make a special effort to choose an optimal (best) D. Stephens and Stitt (1970) demonstrate a way to

select D so that the most representative spectrum is mapped by the analysis. D is the average station separation defined by

$$D = \left\{ \frac{(M-1)(N-1)}{O_i} \right\}^{\frac{1}{2}}, \tag{4.3}$$

where M and N are the number of grid points in the two horizontal coordinate directions and O_i is the number of reports inside the boundaries of the grid.

This approach to estimating the influence radius is best suited for data distributions that are reasonably homogeneous. It is also effective, in slightly altered form, when we encounter extreme data density changes, for example, data rich land areas and data poor water areas.

The algorithm we use is the correction formula

$$A^e_{i,j} = A^g_{i,j} + \sum_{m=1}^{M} \omega_m(R_m,Q_m;D,M) \left\{ O(X_m,Y_m) - A^g(X_m,Y_m) \right\}, \tag{4.4}$$

where M is the number of observations within the influence radius D and the weight function ω_m is normalized to unity by

$$\omega_m(R_m,Q_m;D,M) = C_w(R_m;D)Q_m \Big/ \sum_{\ell=1}^{M} C_w(R_\ell;D)Q_\ell \tag{4.5}$$

Q_m is the relative quality of an observation. We specify the upper air reports and land stations to have equal quality, and ships to have error levels 2.5 times the others, i.e., Q is 1 for land stations and 0.4 for ships.

In equation (4.4), $A^e_{i,j}$ is the new analysis estimate at the (i,j) grid point, and $A^g_{i,j}$ is the preceding analysis estimate or guess if it is the first correction at the (i,j) point. The m^{th} observation with grid coordinates (X_m,Y_m) is denoted $O(X_m,Y_m)$ and the current analysis estimate at (X_m,Y_m) is A^g. The $A^g(X_m,Y_m)$ field is interpolated bilinearly from the grid to the observation sites after all the grid points are corrected. This field is termed the first guess field before the first correction.

During operational processing of the data, we usually receive a high percentage of the possible number of reports. In this case, it is sufficient to use a simple average of the observations as a first guess, $A^g_{i,j}$. In the absence of data in large segments of the grid, the first guess becomes important in determining the final answer. We intend to supply some form of a previously forecasted field as a substitute guess field in this case.

Data outside the grid are valuable in fixing the analysis near the boundaries. They are treated as grid points in the computations. That is, A^g is determined at these observation sites (can't use interpolation--the field average does nicely here) and $A^e(X_m,Y_m)$ is calculated for these sites just as if it were a grid point. The A^e then are the A^g for the next pass.

d. Filtering

Stephens and Polan (1971) show that the successive corrections algorithm produces a field spectrum that approaches the observed. This is true for $D/\lambda < 0.5$ where λ is the wavelength of the (unknown) observed data. Only waves for which $\lambda \geq 2D$ should be present. We enforce this requirement by filtering after each pass.

Near the lateral boundaries, we use the Shuman (1957) filter:

$$\overline{F}_{i,j} = F_{i,j} + \frac{1}{2}\tau(1-\tau)\left\{F_{i+1,j}+F_{i-1,j}+F_{i,j+1}+F_{i,j-1}-4F_{i,j}\right\} + \frac{\tau}{4}^2\left\{F_{i+1,j+1}+F_{i-1,j+1}+F_{i+1,j-1}+F_{i-1,j-1}-4F_{i,j}\right\}, \tag{4.6}$$

where τ is the filter index, and $F_{i,j}$ and $\overline{F}_{i,j}$ are unfiltered and filtered grid values, respectively.

Along the boundaries, we use

$$\overline{F}_{i,j} = F_{i,j} + \frac{1}{2}\tau(F_{-1}-2F_{i,j}+F_{+1}), \tag{4.7}$$

where the + and - indicate the nearest neighbors along the boundary. Corner points are found by taking a weighted average of the corner point and its three nearest neighbors,

$$\overline{F}_c = \left\{F_c + w_1(F_x + F_y) + w_2 F_{xy}\right\} / w_d , \tag{4.8}$$

where F_x, F_y, and F_{xy} are given schematically by

F_c • • F_x

F_y • • F_{xy}

and F_c is the corner. The weights are

$$\left.\begin{aligned} w_1 &= (4D-1)/(4D+1) \\ w_2 &= (4D-\sqrt{2})/(4D+\sqrt{2}) \\ w_d &= 1/(1+2w_1+w_2), \end{aligned}\right\} \tag{4.9}$$

where D is the average station separation.

The interior is filtered by the symmetric, non-recursive filter

$$\overline{F}_{\ell} = \frac{1}{2} \sum_{k=0}^{N} w_k (F_{\ell+k} + F_{\ell-k}). \tag{4.10}$$

This is applied separately in each coordinate direction. The weights and response for the $3\Delta x$ (D=1.5, N=9) filter are shown in figure 4.3.

We have attempted to match the Shuman and interior filter responses for a range of D. The response of the two filters, however, is different. We don't know the effect of this on the forecast model.

e. Special Processing

The potential conflict between pressure and terrain scales was mentioned in Section 3. Here, we just want to add that there is difficulty in being sure what the geostrophic wind really is. There is no way of verifying our estimate. We can make subjective comparisons against the observed winds. Figures 4.4 through 4.7 show the two fields for one map time at the surface and 2000 m levels.

We don't know what effects there are on the model when analyzed winds and geostrophic winds are thrown together without formal initialization.

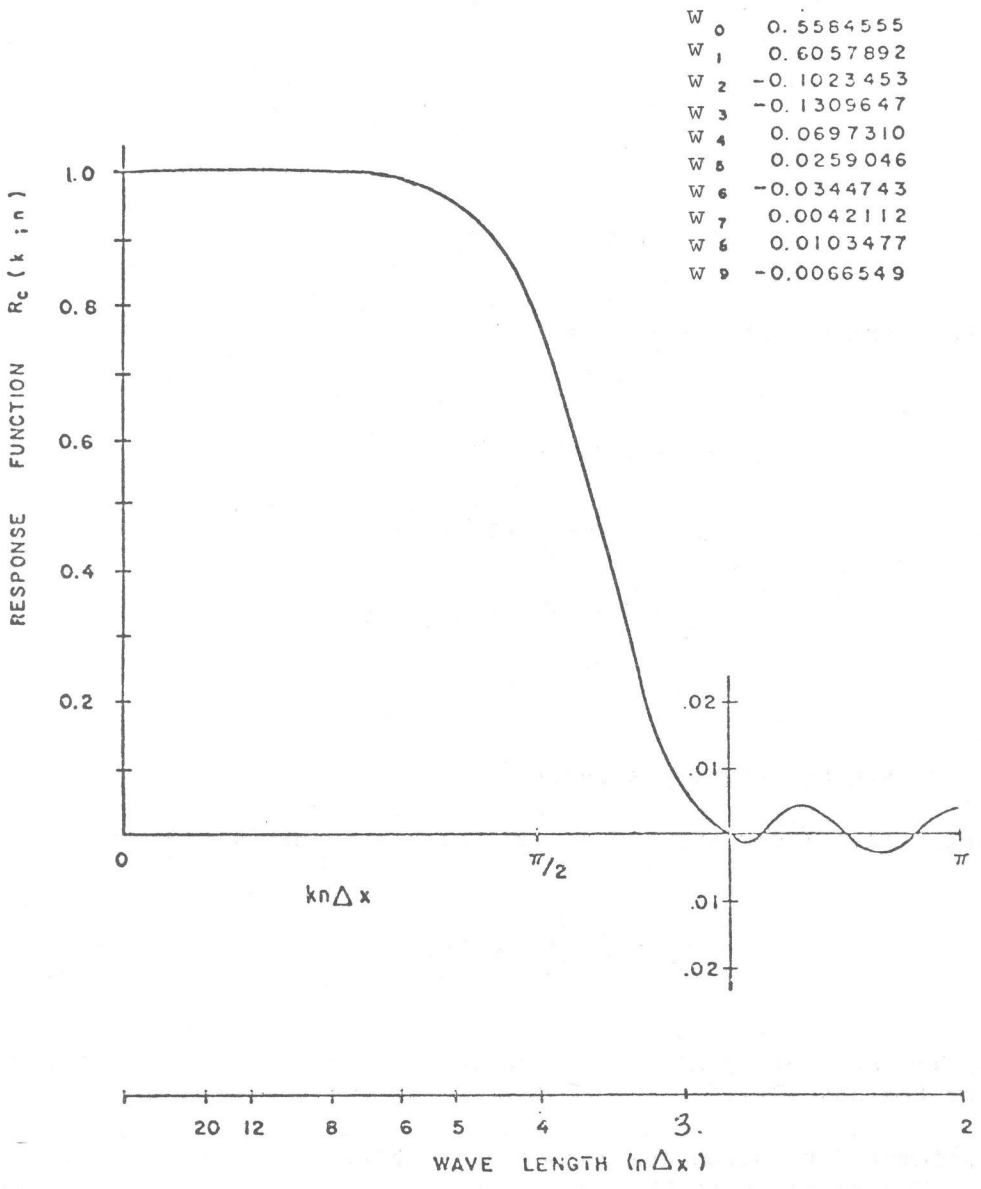

Figure 4.3.--Response function and filter weights for a cutoff wavelength of $3\Delta x$.

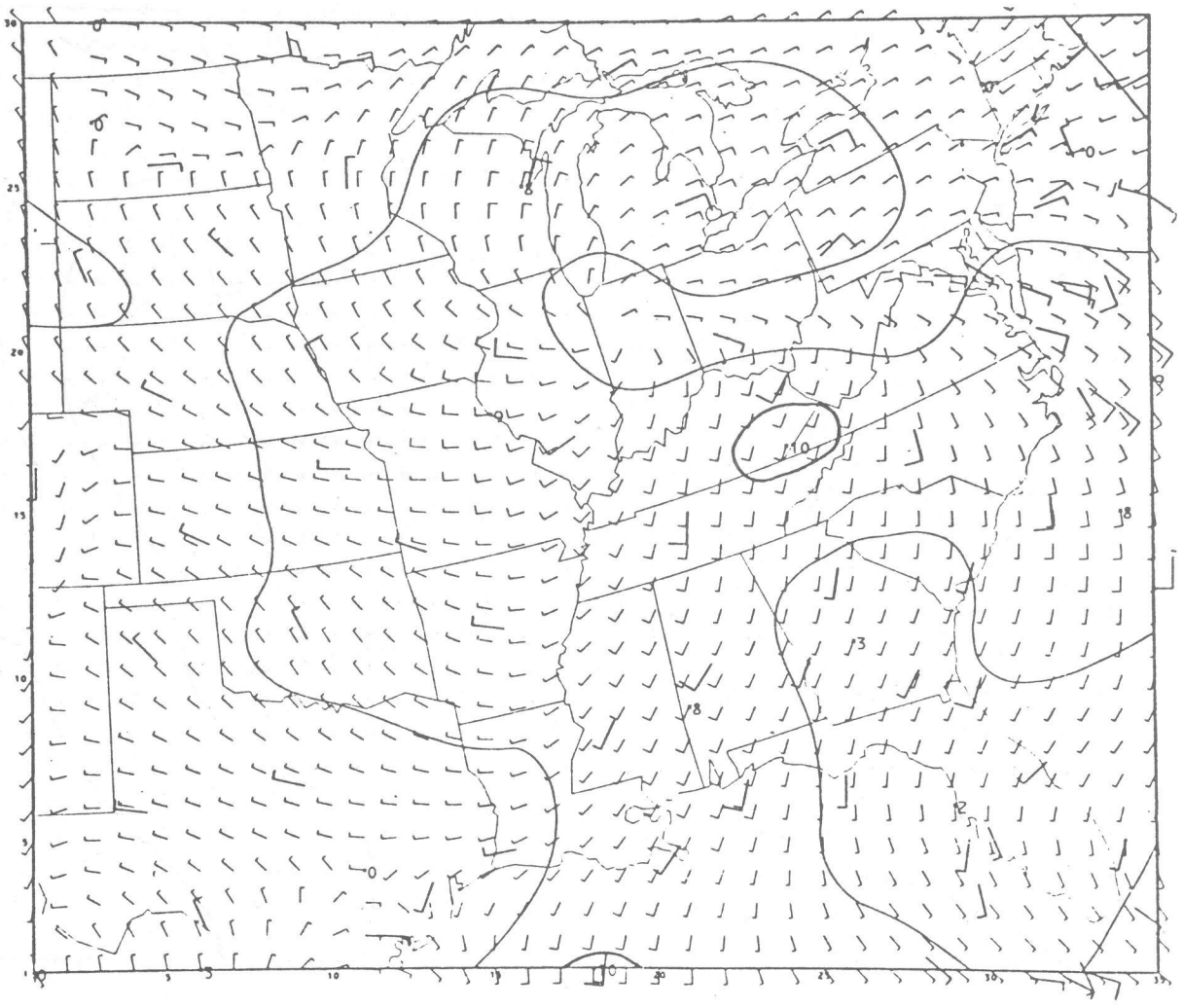

Figure 4.4.--Surface wind analysis and observations for 1200 GMT, March 18, 1977. Separate analyses were performed on the x and y wind components and then recombined to produce the vector wind. The observation barbs are enlarged and originate at station locations. Contours are 5 ms^{-1} isotachs with every 10 ms^{-1} emphasized. Small flags on the barbs represent 5 ms^{-1} and large flags are 10 ms^{-1}. Numbers are grid point relative maxima and minima. Only upper air and ship reports were used. 72 reports were inside the grid. Analysis vector root mean square error is 2.0 ms^{-1} and analysis variance is 90 percent of the observed variance.

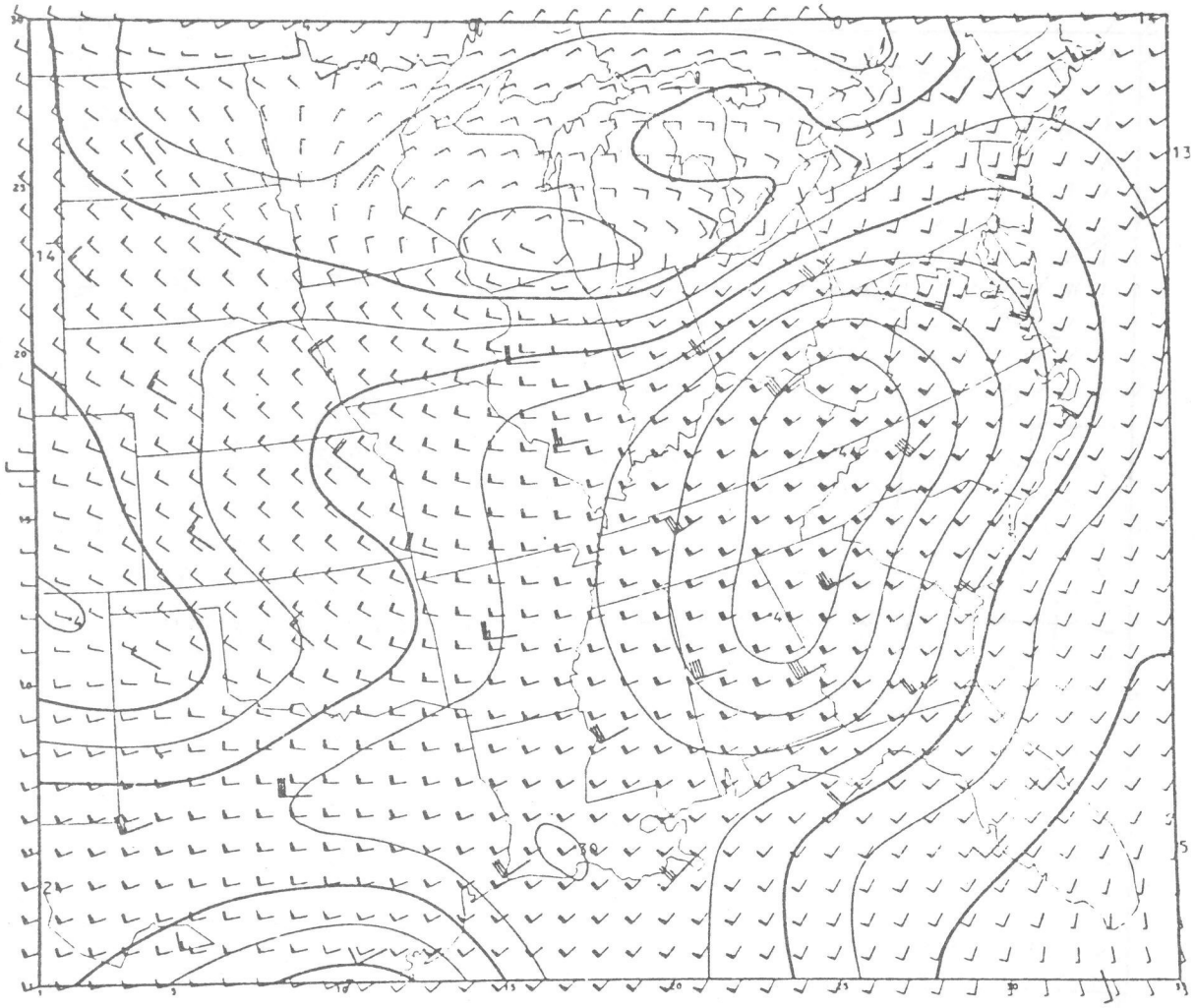

Figure 4.5.--Same as figure 4.4 except level is now 2000 m. The 10 and 20 ms^{-1} isotachs are emphasized. There are 47 reports used in this analysis. Vector root mean square error is 2.33 ms^{-1} and the analysis variance is 98 percent of the observational variance.

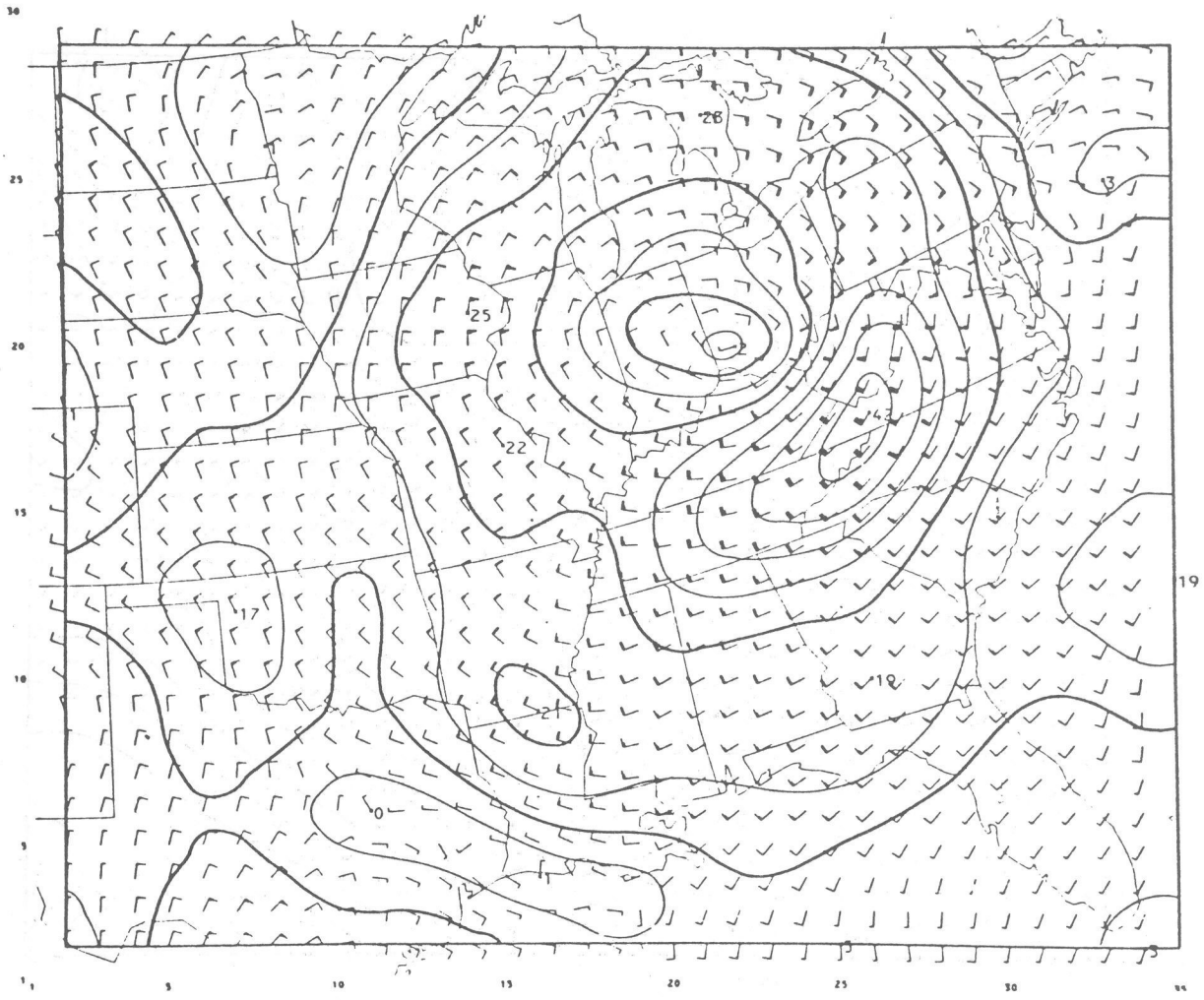

Figure 4.6.--Surface geostrophic wind analysis for 1200 GMT, March 18, 1977. See Section 3e for computational formula. The computation is not performed on boundaries of the (35 x 30) grid.

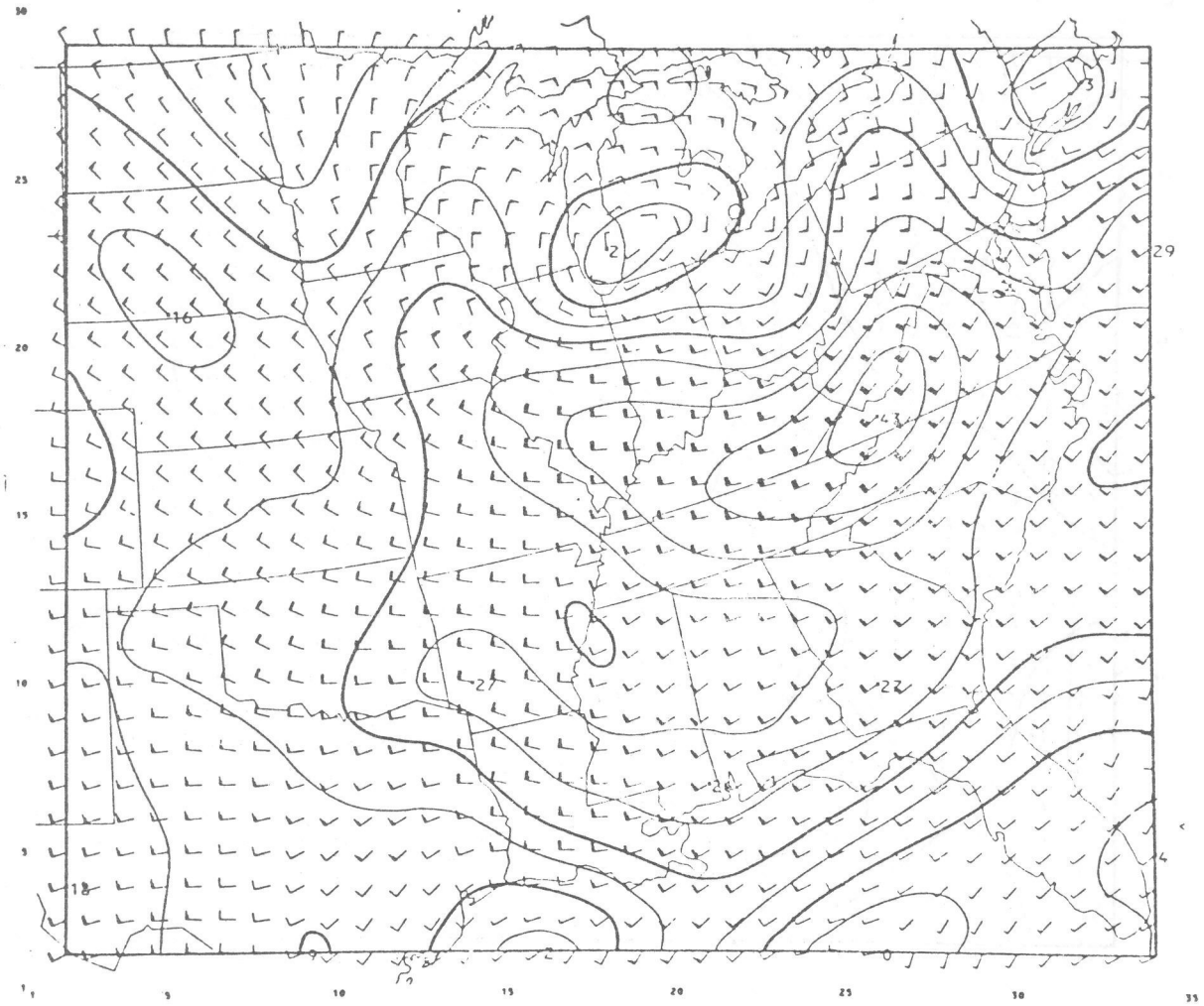

Figure 4.7.--Same as figure 4.6 except level is 2000 m.

There is only one upper air sounding available in the water areas--ship H in the North Atlantic. The Gulf of Mexico and the rest of the Atlantic is sampled only at the surface. When we analyze each model level independently, we infer the field estimates over the water from land based reports. This can lead to unrealistic temperature profiles in the water areas. We adjust the profile in these areas by first fixing the surface level to the sea surface temperature. Currently, we use the satellite sea surface temperature estimates. At each grid point over water, we assume a dry adiabatic lapse rate holds until we intersect the original independently produced analyzed sounding. The analyzed sounding is maintained thereafter. We do not adjust for potential saturation nor do we adjust the moisture profile except to insure that the dewpoint never exceeds the temperature.

There are schemes we want to test to improve upon this crude attempt to represent the marine atmosphere. We also want to test the effects of the marine adjustments upon the implied coastal boundaries and the resulting forecast.

We now filter the adjusted fields to the same limiting resolvable scale as in the original temperature analysis. This limits the intensity of the coastline gradients. Figure 4.1 shows the original surface temperature as defined by ships and land reports. Figure 4.8 shows the effects on the temperatures when we superimpose the sea-surface temperatures and then filter the field. Figure 4.2 shows the initial 50 m level temperature for this same case, and figure 4.9 shows the adjusted and filtered field.

The cloud field is the last one we treat. We analyze the surface observed cloud amounts limiting the results to lie between 0 and 100 percent coverage.

MOS cloud forecasts are treated as cloud observations for the rest of the required forecast times, and these are similarly analyzed. We would eventually like to include digitized satellite observed cloudiness in our initial specification.

5. VERIFICATION OF THE BOUNDARY LAYER MODEL'S FORECASTS

a. Basics

The verification program compares statistically the boundary layer model's forecasts with observed data. The program also compares the LFM model with observations and BLM forecasts. Comparisons with MOS and trajectory forecast models are being added. All verification is done at observation sites, with forecasts interpolated bilinearly to the sites. Further details of the verification program along with comparisons with the LFM, MOS, and trajectory models will appear in a future report.

b. Wind Verification

The observed u-component and v-component of the winds are transformed to the BLM grid (i.e., transformed to a polar stereographic reference frame)

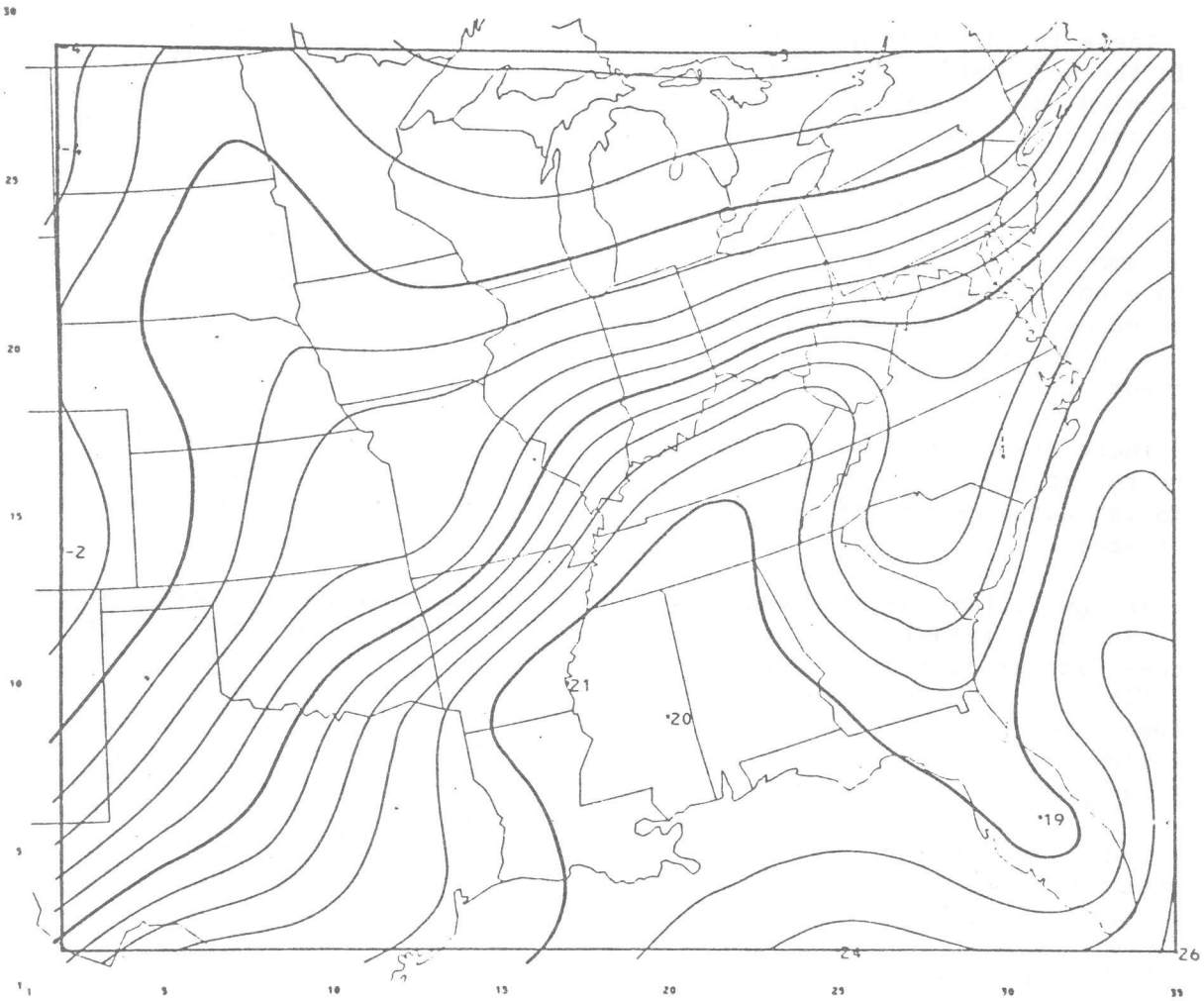

Figure 4.8.--Marine adjusted surface temperature analysis for 1200 GMT, March 18, 1977. Compare with figure 4.1. Analysis has been filtered to be consistent in scale resolution to that given by just the upper air and ship reports.

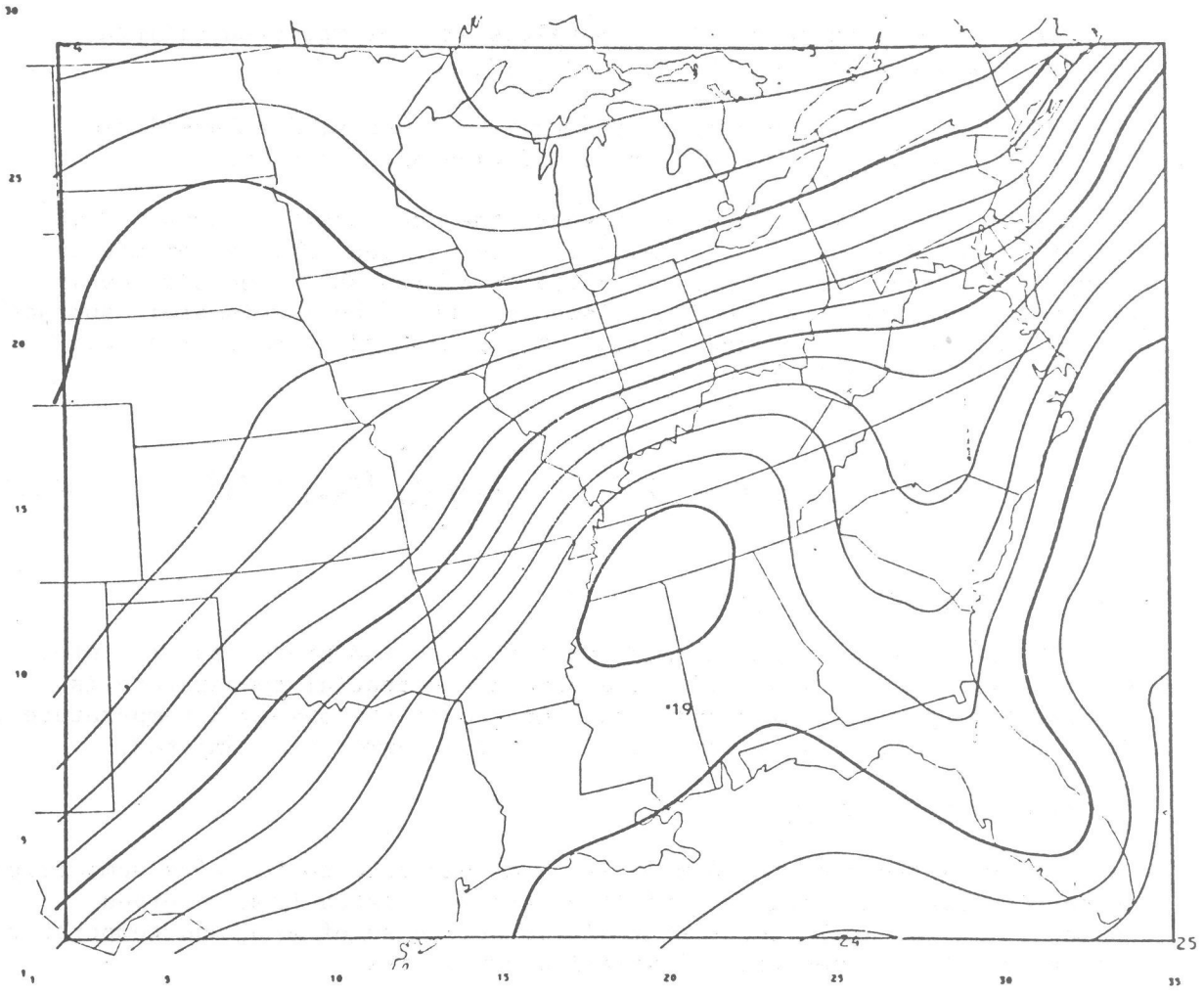

Figure 4.9.--Marine adjusted and filtered 50-m temperature analysis. Compare with figure 4.2. Note change in the analysis over the water and in the Florida peninsula area. Filter is the same one used in the original analysis (fig. 4.2).

before comparisons are made. The BLM values are interpolated bilinearly to the observation points from the 35 x 30 grid.

For each model level, we compute the average u and v, mean absolute error, bias, r.m.s. wind vector error, and wind direction error.

The LFM boundary layer output represents the atmosphere's lowest 50 mb. In order to compare the BLM forecasts to those of the LFM, we compute an integrated average over the first six levels of the BLM. The six levels approximately represent the model's lowest 50 mb. The levels are: surface, 50 m, 110 m, 190 m, 305 m, and 465 m. The integrated average of a variable f_i follows the trapezoidal rule,

$$\bar{f} = \frac{1}{2} \sum_{i=1}^{5} (f_i + f_{i+1}) (z_{i+1} - z_i) \Big/ \sum_{i=1}^{5} (z_{i+1} - z_i). \qquad (5.1)$$

c. Temperature Verification

The BLM potential absolute temperatures and the BLM pressures are interpolated to the observation grid. The absolute potential temperature is converted to degrees Celsius and then compared to the observed temperatures. As with the wind, mean absolute error and r.m.s. error are computed.

d. Humidity Verification

The BLM-predicted specific humidities are converted to relative humidities. Station relative and absolute humidities are calculated from observed dewpoints. Statistical comparisons similar to those of wind and temperature are carried out for specific and relative humidities.

ACKNOWLEDGMENTS

The authors thank Ms. Barbara Howerton for her attention to detail and the typing of several drafts of the manuscript and Dr. M. A. Alaka for his editorial assistance in the preparation of this report.

REFERENCES

Atwater, M. A., 1970: Investigation of the radiation balance for polluted layers of the urban environment. Ph.D. Thesis, New York University, New York, 141 pp.

Bergthorsson, P., and B. Doos, 1955: Numerical weather map analysis. Tellus, 7, 329-340.

Businger, J. A., J. C. Wyngaard, Y. Izumi, and E. F. Bradley, 1971: Flux-profile relationships in the atmospheric surface layer. J. Atmos. Sci., 28, 181-189.

Carslaw, H. S., and J. C. Jeager, 1959: Conduction of Heat in Solids. Oxford University Press, London, England, 510 pp.

Deardorff, J. W., 1971: Rate of growth of the nocturnal boundary layer. Presented at the Symposium on Air Pollution, Turbulence and Diffusion, Las Cruces, New Mexico, NCAR ms. No. 71-246.

Deardorff, J. W., 1974: Three-dimensional numerical study of the height and mean structure of a heated boundary layer. Boundary Layer Meteorology, 7, 81-106.

Fankhauser, J. C., 1974: The derivation of consistent fields of wind and geopotential from mesoscale rawinsonde data. J. Appl. Meteor., 13, 637-646.

Gandin, L. S., 1963: Objective analysis of meteorological fields. Leningrad, Hydrometeor. Publ. House (English version, Israel Program for Science Translations, 1965), 242 pp.

Gerrity, J. P., 1967: A physical-numerical model for the prediction of synoptic-scale low cloudiness. Mon. Wea. Rev., 95, 261-282.

Halstead, M. R., R. Richman, W. Covery, and J. Merrman, 1957: A preliminary report on the design of a computer of micrometeorology. J. Meteor., 14, 308-325.

Long, P. E., 1978: A modeler's guide to simple numerical filters. NOAA Technical Memorandum (in preparation).

Long, P. E., 1978: Numerical diffusion schemes for long time-step integrations of numerical boundary layer models. TDL Office Note (in preparation).

Long, P. E., and D. W. Pepper, 1976: A comparison of six numerical schemes for calculating the advection of atmospheric pollution. Preprints Third Symposium on Atmospheric Turbulence, Diffusion and Air Quality, AMS Conference, Oct 19-22, 1976, Raleigh, N.C., 181-187.

Long, P. E., and F. J. Hicks, 1975: Simple properties of chapeau functions and their application to the solution of the advection equation. TDL Office Note 75-8, National Weather Service, NOAA, Silver Spring, Md., 33 pp.

Long, P. E., and W. A. Shaffer, 1973: Some physical and numerical aspects of boundary layer modeling. Presented at the Second Conference on Numerical Prediction, Oct. 1-4, Monterey, California. Available as a NOAA Technical Memorandum NWS TDL-56, Silver Spring, Md., 1975, 37 pp.

O'Brien, J. J., 1970: A note on the vertical structure of the eddy exchange coefficient in the planetary boundary layer. J. Atmos. Sci., 27, 1213-1215.

Obukhov, A. M., 1946: Turbulence in an atmosphere with a non-uniform temperature. Trudy Instituta Teoreticheskio Geofiziki ANSSR. Translated and reprinted in Boundary Layer Meteorology, 2, 1971, 3-29.

Pandolfo, J. P., M. A. Atwater, and G. E. Anderson, 1971: Prediction by numerical models of transport and diffusion in an urban boundary layer. The Center for the Environment of Man, Inc., Hartford, Conn., 139 pp.

Shaffer, W. A., 1978: A simple soil heat flux calculation. NOAA Technical Memorandum (in preparation).

Shaffer, W. A., and P. E. Long, 1973: A predictive boundary layer model. Presented at the Symposium on the Atmospheric Boundary Layer, Oct. 10-12, 1973, Mainz, Germany. Available as a NOAA Technical Memorandum NWS TDL-57, Silver Spring, Md., 1975, 44 pp.

Shuman, F. G., 1957: Numerical methods in weather prediction: II. Smoothing and filtering. Mon. Wea. Rev., 85, 357-361.

Smithsonian Institution, 1951: Smithsonian Meteorological Tables. City of Washington, 6th Revised edition, 527 pp.

Stephens, J. J., and A. L. Polan, 1971: Spectral modification by objective analysis. Mon. Wea. Rev., 99, 374-378.

Stephens, J. J., and J. M. Stitt, 1970: Optimum influence radii for interpolation with the method of successive corrections. Mon. Wea. Rev., 98, 680-687.

Tennekes, H., 1973: A model for the dynamics of the inversion above a convective boundary layer. J. Atmos. Sci., 30, 558-567.

U. S. Department of Agriculture, 1958: Major land uses in the United States. U. S. Government Printing Office, 471954.

U. S. Department of Interior, 1967: Distribution of principal kinds of soils: orders, suborders, and great groups. U. S. Geological Survey, Sheet No. 89.

Webb, E. K., 1970: Profile relationships: The log-linear range, and extension to strong stability. Quart. J. R. Met. Soc., 96, 67-90.

Yanenko, N. A., 1971: The Method of Fractional Steps. Springer-Verlag, Heidelberg, 160 pp.

APPENDIX A. Reprinted from Shaffer and Long, 1973.

LONG WAVE RADIATION FLUX

Long wave radiation and atmospheric heating due to its flux divergence are calculated for each time step of the model. Account is taken of cloud cover in the model and both water vapor and carbon dioxide are considered as emitters of long wave radiation. For water vapor, an increment of optical path length in a layer, dW_{H_2O}, which has density ρ and specific humidity q, is given by

$$dW_{H_2O} = \rho q \, dz$$

Once these increments of optical path length are obtained, they are summed from the top of the boundary layer to the i^{th} level to give the path length, W_i

$$W_{H_2O}(i) = \sum_{j=1}^{\text{Top of B.L.}} dW_{H_2O}.$$

The emissivity function for water vapor being used was derived by Kuhn (1963) using atmospheric temperature, humidity and long wave radiation measurements. These emissivities, as given in Pandolfo et al. (1971), are

$$E_{i,j} = \begin{cases} 0.1129 \log_{10}(1 + 12.63u) & \text{for } \log_{10} u \leq -4 \\ 0.104 \log_{10} u + 0.440 & \log_{10} u \leq -3 \\ 0.121 \log_{10} u + 0.491 & \log_{10} u \leq -1.5 \\ 0.146 \log_{10} u + 0.527 & \log_{10} u \leq -1 \\ 0.161 \log_{10} u + 0.520 & \log_{10} u \leq 0 \\ 0.136 \log_{10} u + 0.542 & \log_{10} u > 0 \end{cases}$$

where $u = |W_i - W_j|$ is the optical path length between the i^{th} and j^{th} level

In addition to the emission of long wave radiation by water vapor, carbon dioxide emission is considered. Basically the 15-cm band is the only band of significance for CO_2, so emissivities and path length are based on it. No interaction effects between CO_2 and H_2O vapor are considered here (Atwate 1970). Pandolfo's path lengths are used for CO_2

$$dW_{CO_2} = 0.4148 \, (p_i - p_{i+1}) \text{ cm/atmos.}$$

which assume a constant CO_2 concentration throughout the atmosphere. The emissivity is given as

$$E_{CO_2}(i,j) = 0.185 \left[1 - \exp\left(-.3919 |W_{CO_2}(i) - W_{CO_2}(j)|^{0.4}\right)\right].$$

a. Downward Long Wave Flux

The downward flux of long wave radiation at a reference level, j_r, is the sum of the emissions for each layer above, modified by absorption between the layer and j_r, plus the amount of radiation reaching j_r from above the boundary layer. The flux reaching the top of the boundary layer is now assumed to be σT^4_{ABOVE}. (This flux will be calculated in the 3-dimensional model using temperatures and humidities from the large-scale model that supplied dynamic boundary conditions for the model.) Clouds, except cirrus, may be present in any layer and are assumed to radiate as black bodies. Cirrus radiate as "half-black" bodies.

With these assumptions, the downward flux at a level j_r can be expressed as (see figure A.1)

$$F_{j_r} = \sum_{j=j_r}^{top-1} \left[\frac{\sigma}{2} \left(T^4_{j+1} + T^4_{j} \right) \left(E(j_r, j+1) - E(j_r, j) \right) C_{jr,\, j} + \sigma\, T_j^4\, (1 - E(j_r, j))\, c_j\, C_{jr,\, j+1} \right] + \sigma\, T^4_{ABOVE} \left[(1 - E(j_r, Top) \right] C_{j_r,\ \text{Top of B.L.}}$$

where $C_{i,j}$ = fraction of clear sky between levels i and j and c_j= fraction of clouds in layer j.

b. Upward Long Wave Flux

The upward flux at any level consists of the amount of reflected long wave flux that is transmitted to the level, plus the amount of radiation emitted below which reaches the level. If ε_S is the surface emissivity (it is not necessary to have a "black" surface), the reflected flux at the surface is

$$F_{refl} = F_{sfc}(1-\varepsilon_S).$$

The upward flux at level j_r can be expressed as

$$F_{j_r} = \sum_{j=2}^{jr} \left[\frac{\sigma}{2} \left(T^4_{j-1} + T^4_{j} \right) \left(E(j_r, j-1) - E(j_r, j) \right) C_{jr,\, j-1} + \sigma\, T_j^4\, (1 - E(j_r, j))\, c_j\, C_{jr,\, j} \right] + (\varepsilon_s\, \sigma\, T^4_{sfc} + F_{refl})\, [1 - E(j_r, sfc)]\, C_{jr,\, sfc}.$$

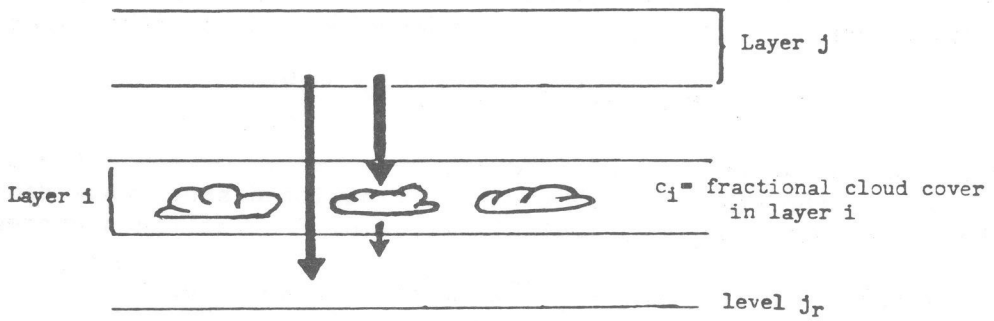

The amount of downward flux reaching j_r from layer j is

$$\sigma T_j^4 \Delta E_j (1-c_i)$$

The amount of flux reaching j_r from layer i is

$$\sigma T_i^4 \Delta E_i (1-c_i) + \sigma T_{\substack{\text{cloud} \\ \text{base}}}^4 c_i (1-E(\text{cloud base}, j_r))$$

Figure A.1.--Treatment of long wave radiation, including clouds within the boundary layer.

APPENDIX B. Reprinted from Shaffer and Long, 1973.

SHORT WAVE RADIATION FLUXES

Incident on the top of the atmosphere is the solar flux, S_o, of roughly 2.0 cal/cm^2/min. Part of this flux is absorbed due to water vapor and other absorbers in the atmosphere and part is scattered back to space. An expression from McDonald (1960) gives the absorption due to water vapor as

$$A_w = 0.077 \ (U_{Above} \sec Z)^{0.3}$$

where U_{Above} is the optical path length of water vapor above the boundary layer and Z is the solar zenith angle. Transmitted short wave radiation in the absence of water vapor is calculated using Kondrat'yev's expression

$$\tau = 1.041 - 0.16 \left[(0.949 \frac{P_{Top\ of\ B.L}}{P_{surface}} + 0.051) \sec Z \right]^{1/2}$$

which accounts for scattering. The short wave radiation to reach the top of the boundary layer is

$$S_{BL} = \begin{cases} S_o \cos Z \ (\tau - A_w) \ ; & \cos Z > 0 \\ 0 & \text{otherwise} \end{cases}.$$

Clouds appearing above the boundary layer are broken into three categories—high, middle, and low. The fractional covering of each will be estimated from large-scale model humidities. Clouds within the boundary layer make up a fourth class and will eventually be predicted using boundary layer model predicted humidities. Each cloud category has a transmission function (Pandolfo et al. 1971) associated with it:

$$T_{Boundary\ Layer} = 0.25\text{-}0.01 \sec Z$$

$$T_{Low} = 0.35\text{-}0.015 \sec Z$$

$$T_{Middle} = 0.45\text{-}0.01 \sec Z$$

$$T_{High} = 0.9\text{-}0.04 \sec Z$$

where T is the fraction tramsmitted. When clouds are included in the model above the boundary layer, the short wave flux at the boundary layer top becomes

$$S_{BL} = S_{BL}\ (\text{No clouds}) \prod_{i=1}^{3} [1 - C_i \ (1 - T_i)]$$

where C_i is the fractional covering in the i^{th} category (figure B.1).

Within the boundary layer, Pandolfo's expressions for absorption by water vapor and for scattering are used:

$$di_{H_2O} = - 7.55 \times 10^{-4} \ (u \sec Z)^{- 0.7} \ du$$

$$di_{scatt} = - 2 \ S_o \ (3.796 \times 10^{-5}) \left[(0.949 \frac{P_i}{P_o} + 0.051) \sec Z\right]^{-1/2} (P_i - P_{i-1}).$$

The short wave radiation which finally reaches the surface is

$$I_{Surface} = \left[S_{BL}(\text{With clouds}) + \sum_{j=1}^{\text{Top of B.L}} (di_{H_2O} + di_{scatt})_j\right] \times (1 - c_{BL} \ (1 - T_{BL}))$$

where c_{BL} is the fraction of cloud cover within the boundary layer. The amount of radiation absorbed at the surface is

$$I \underset{\text{surface}}{\text{abs. at}} = (1 - \text{albedo}) \ I_{surface}.$$

No account is made of reflected short wave radiation or its heating.

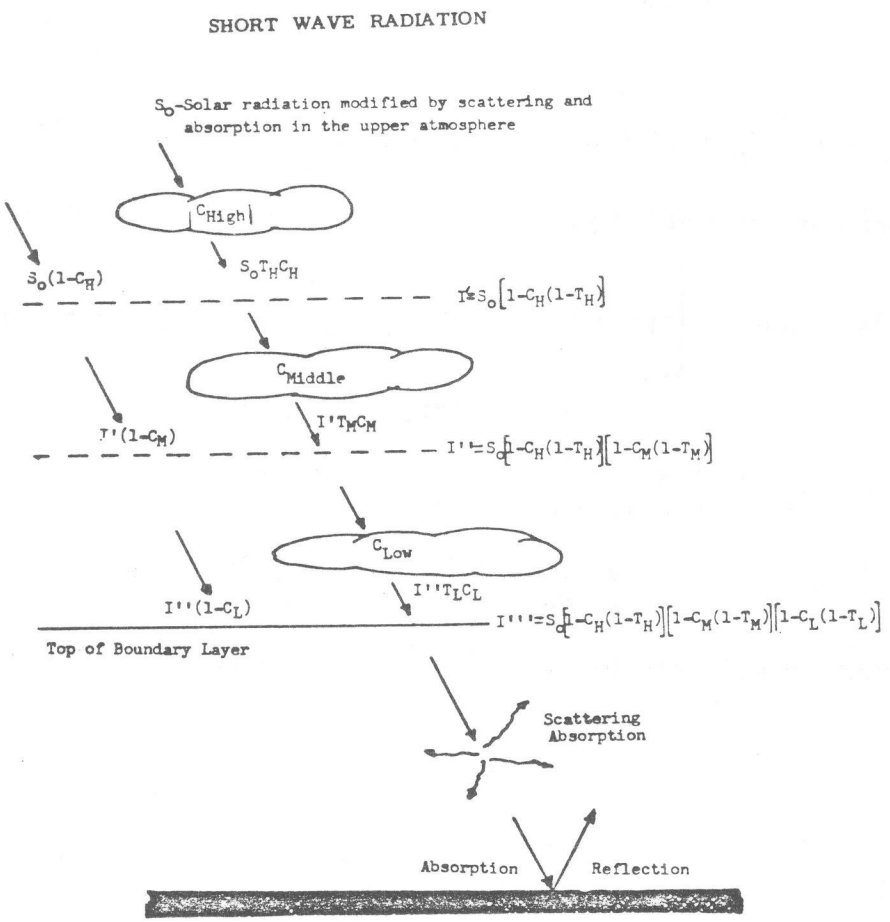

Figure B.1.--Treatment of solar radiation.

APPENDIX C. Reprinted from Shaffer and Long, 1973.

SOIL HEAT FLUX

An analytic solution of the heat equation is used to calculate soil heat flux. Two basic assumptions are made: 1) the soil thermal coefficients do not vary with depth and 2) the initial soil temperature profile is known. In order to solve the heat equation, two boundary conditions are necessary. At the air-soil interface, a heat flux F(t) enters the soil. The second condition is that the soil temperature approaches a constant value as the depth is increased. Measurements show that soil temperature varies little below 1 or 2 meters over a 24-hour period, justifying the use of this assumption.

Use of these assumptions in the heat equation gives the temperature at depth Z (positive downward) at time t as

$$T_{soil}\ (Z,\ t) = \frac{1}{2\sqrt{\pi\ k\ t}} \int_0^\infty f_o(\zeta) \left\{ e^{-(Z-\zeta)^2/(4kt)} + e^{-(Z+\zeta)^2/(4kt)} \right\} d\zeta$$

$$+ \frac{1}{K} \sqrt{\frac{k}{\pi}} \int_0^t e^{-Z^2/(4\ k\ u)}\ \frac{F(t-u)}{\sqrt{u}}\ du$$

where $f_o(z)$ is the initial soil temperature profile, F(t) is the surface soil heat flux, K is the thermal conductivity k is the thermal diffusivity and u is a dummy variable. (See Carslaw and Jeager (1959) for example, for a derivation of the above equation.) Only the surface temperature is of interest; at the surface the temperature reduces to

$$T_{sfc}\ (t) = \frac{1}{\sqrt{\pi\ k\ t}} \int_0^\infty f_o\ (\zeta)\ e^{-\zeta^2/4\ kt}\ d\zeta$$

$$+ \frac{1}{K} \sqrt{\frac{k}{\pi}} \int_0^t \frac{F\ (t-u)}{\sqrt{u}}\ du\ .$$

The first term on the right-hand side is due to redistribution of heat associated with the initial soil temperature profile. The profile is simply integrated with a Gaussian. Solutions for this term using several useful, simple profiles are given in Table C.1.

The second term of the soil heat flux equation above is caused by fluxes occuring after t=0. In order to evaluate this term, the flux during each model time step, Δt, is assumed to be linear in time. (Note: The term can also be evaluated by assuming that the soil heat flux is constant during each step. Only a slight change in the final coefficients results.) At time $t = n\Delta t$, the flux that occurred between time $i\Delta t$ and $(i+1)\Delta t$ can be written as

$$F = F_{n-i} - \left(\frac{F_{n-i} - F_{n-i-1}}{\Delta t}\right)(u - i\Delta t).$$

Integration during each interval, then summing yields the second term:

$$\frac{4}{3}\sqrt{\frac{k\Delta t}{\pi K^2}}\left\{F_n + \sum_{i=1}^{n-1}\left[(i+1)^{3/2} + (i-1)^{3/2} - 2i^{3/2}\right]F_{n-i} + \left[(n-1)^{3/2} - n^{3/2} + \frac{3}{2}\sqrt{n}\right]F_0\right\}.$$

As an example, if a constant initial temperature profile with the initial flux, F_0, equal to zero, is assumed, the surface temperature can be written as

$$T_{sfc}(t = n\Delta t) = T_\infty + \frac{4}{3}\sqrt{\frac{k\Delta t}{\pi K^2}}\left[F_n + \sum_{i=1}^{n-1} C_i F_{n-i}\right].$$

Inverting the equation for the soil heat flux, the flux is linear in the surface temperature

$$F_n = \frac{3}{4}\sqrt{\frac{\pi K^2}{k\Delta t}}\,(T_{sfc} - T_\infty) - \sum_{i=1}^{n-1} C_i F_{n-i} = C\,T_{sfc} + C'.$$

This form is readily adapted to the energy balance used to solve for surface temperature.

Table C.1.-- Evaluation of the soil heat term due to various initial profiles.

Initial Soil Heat Profile	$\frac{1}{\sqrt{\pi kt}} \int_o^\infty f_o(\zeta)\, e^{-\zeta^2/4\,kt}\, d\zeta$
$f_o = T_\infty$ (constant)	T_∞
$f_o = Ae^{-BZ_{soil}}$ (exponential)	$Ae^{B^2kt}\ \mathrm{erfc}\ (B\sqrt{kt})$
$f_o = Ae^{-BZ^2_{soil}}$ (Gaussian)	$A\,(1 + 4\,Bkt)^{-1/2}$

APPENDIX D

NUMERICAL SCHEMES FOR ADVECTION AND DIFFUSION

a. Advection

The linear chapeau function solution to the advection relation with a forcing function, g(x,t),

$$\frac{\partial Q}{\partial t} + u(x,t)\,\frac{\partial Q}{\partial x} = g(x,t) \tag{D.1}$$

is found by solving

$$A_j\, Q_{j-1}^{n+1} + B_j\, Q_j^{n+1} + C_j\, Q_{j+1}^{n+1} = D_j\ , \tag{D.2}$$

in which A, B, C and D are given by

$$\left.\begin{aligned}
A_j &= h_- - \Delta t/2\ (2u_j + u_{j-1}) \\
B_j &= 2(h_- + h_+) - \Delta t/2\ (u_{j+1} - u_{j-1}) \\
C_j &= h_+ + \Delta t/2\ (2u_j + u_{j+1}) \\
D_j &= h_-\, Q_{j-1}^n + 2(h_- + h_+)\, Q_j^n + h_+\, Q_{j+1}^n \\
&\quad - \Delta t/2\ (2u_j + u_{j+1})\, Q_{j+1}^n + \Delta t/2\ (2u_j + u_{j-1})\, Q_{j-1}^n \\
&\quad + \Delta t/2\ (u_{j+1} - u_{j-1})\, Q_j^n \\
&\quad + \Delta t \left[h_-\, g_{j-1} + 2(h_- + h_+)\, g_j + h_+\, g_{j+1}\right] .
\end{aligned}\right\} \tag{D.3}$$

If gridpoint N is an outflow boundary, where outflow is defined by $2u_N + u_{N-1} > 0$, then we can write a prediction equation for gridpoint N,

$$
\left.
\begin{aligned}
A_N &= h_- - \Delta t/2\ (2u_N + u_{N-1}) \\
B_N &= 2h_- + \Delta t/2\ (2u_N + u_{N-1}) \\
C_N &= 0 \\
D_N &= h_-\ Q^n_{N-1} + 2h_-\ Q^n_N + \Delta t/2\ (2u_N + u_{N-1})\ Q^n_{N-1} \\
&\quad - \Delta t/2\ (2u_N + u_{N-1})\ Q^n_N + \Delta t h_-\ (2g_N + g_{N-1}).
\end{aligned}
\right\} \qquad (D.4)
$$

Similarly, if j = 1 is an outflow point, we have

$$
\left.
\begin{aligned}
A_1 &= 0 \\
B_1 &= 2h_+ - \Delta t/2\ (2u_1 + u_2) \\
C_1 &= h_+ + \Delta t/2\ (2u_1 + u_2). \\
D_1 &= 2h_+\ Q^n_1 + h_+\ Q^n_2 + \Delta t/2\ (2u_1 + u_2)\ (Q^n_1 - Q^n_2) + \Delta t h_+\ (2g_1 + g_2).
\end{aligned}
\right\} \qquad (D.5)
$$

In (D.3), we use $h_+ \equiv x_{j+1} - x_j$ and $h_- \equiv x_j - x_{j-1}$.

b. Diffusion

The linear finite element (chapeau) solution of the diffusion equation,

$$
\frac{\partial Q}{\partial t} = \frac{\partial}{\partial z}\left(K \frac{\partial Q}{\partial z}\right), \qquad (D.6)
$$

is the same form as (D.2), with

$$
\left.
\begin{aligned}
A_j &= \Delta z_- - 3(K_j + K_{j-1})\,\Delta t/2\Delta z_- \\
B_j &= 2(\Delta z_- + \Delta z_+) + 3\Delta t/2 \\
&\quad \left[K_{j-1}/\Delta z_- + \left(\frac{1}{\Delta z_-} + \frac{1}{\Delta z_+}\right) K_j + K_{j+1}/\Delta z_+\right] \\
C_j &= \Delta z_+ - 3(K_j + K_{j+1})\,\Delta t/2\Delta z_+ \\
D_j &= \left[3(K_j + K_{j-1})\,\Delta t/2\Delta z_- + \Delta z_-\right] Q^n_{j-1} \\
&\quad + \left\{2(\Delta z_- + \Delta z_+) - \frac{3\Delta t}{2}\left[K_{j-1}/\Delta z_- + \left(\frac{1}{\Delta z_-} + \frac{1}{\Delta z_+}\right) K_j + K_{j+1}/\Delta z_+\right]\right\} Q^n_j \\
&\quad + \left[3(K_j + K_{j+1})\,\Delta t/2\Delta z_+ + \Delta z_+\right] Q^n_{j+1}\,.
\end{aligned}
\right\} \quad (D.7)
$$

Equation (D.7) assumes that K is defined at the same levels as z_j and that $h_+ \equiv z_{j+1} - z_j$ and $h_- \equiv z_j - z_{j-1}$.

The 4th-order scheme (refers to spatial accuracy when K and Δz are constant) is given by

$$
\left.
\begin{aligned}
A_j &= \Delta z_-/6 - K_-\Delta t/\Delta z_- \\
B_j &= (\Delta z_- + \Delta z_+)/3 + (K_-/\Delta z_- + K_+/\Delta z_+)\Delta t \\
C_j &= \Delta z_+/6 - K_+\,\Delta t/\Delta z_+ \\
D_j &= \Delta z_-\, Q^n_{j-1}/6 + \Delta z_+\, Q^n_{j+1}/6 + (\Delta z_- + \Delta z_+)\, Q^n_j/3\,.
\end{aligned}
\right\} \quad (D.8)
$$

The 4th-order scheme damps $2\Delta z$ waves by a factor of $1/(1 + 12\sigma)$ when K and Δz are constant. The Fourier number, σ, is defined by $\sigma \equiv K\Delta t/\Delta z^2$.

The damping diffusion scheme eliminates all $2\Delta z$ waves when K and Δz are constant. For arbitrary Δz and K, the scheme is

$$
\left.
\begin{aligned}
A_j &= \Delta z_-/4 - K_-\Delta t/\Delta z_- \\
B_j &= (\Delta z_+ + \Delta z_-)/4 + (K_-/\Delta z_- + K_+/\Delta z_+)\Delta t \\
C_j &= \Delta z_+/4 - K_+\Delta t/\Delta z_+ \\
D_j &= \Delta z_- \, Q^n_{j-1}/4 + (\Delta z_- + \Delta z_+)\, Q^n_j/2 + \Delta z_+ \, Q^n_{j+1}/4 \, .
\end{aligned}
\right\} \qquad (D.9)
$$

The 4th order and damping diffusion schemes assume that K is defined midway between levels. We use the notation,

$$
\left.
\begin{aligned}
K_+ &\equiv K(z_+) \qquad & z_+ &= (z_j + z_{j+1})/2 \\
K_- &\equiv K(z_-) \qquad & z_- &= (z_j + z_{j-1})/2 \, .
\end{aligned}
\right\} \qquad (D.10)
$$

APPENDIX E

SURFACE LAYER RELATIONS

a. Unstable Lapse Rate

The integration of the Businger relations (defined by 2.11 and 2.12) yields

$$F(L) = .74 \ln \left[\frac{(q_h - 1)(q_o + 1)}{(q_h + 1)(q_o - 1)} \right] \tag{E.1}$$

$$G(L) = \ln \left[\frac{(r_h - 1)(r_o + 1)}{(r_h + 1)(r_o - 1)} \right] + (\tan^{-1} r_h - \tan^{-1} r_o) \tag{E.2}$$

in which

$$\left.\begin{aligned} q_h &= (1 - 9\, h/L)^{\frac{1}{2}} \\ q_o &= (1 - 9\, z_o/L)^{\frac{1}{2}} \end{aligned}\right\} \tag{E.3}$$

and

$$\left.\begin{aligned} r_h &= (1 - 15\, h/L)^{\frac{1}{4}} \\ r_o &= (1 - 15 z_o/L)^{\frac{1}{4}} \end{aligned}\right\} \tag{E.4}$$

b. Stable Lapse Rate

The integration of the Businger relations for stable conditions ($L \geq 0$) yields

$$F(L) = .74 \left[\ln (h/z_o) + 6.35 (h - z_o)/L \right] \tag{E.5}$$

$$G(L) = \ln (h/z_o) + 4.7 (h - z_o)/L \tag{E.6}$$

Relations (E.5), E.6) and 2.13) can be cast into a quadratic equation. Its solution is

$$L = \frac{\left[-b + (b^2 - 4ac)^{\frac{1}{2}} \right]}{2a} \tag{E.7}$$

in which

$$\left.\begin{aligned} a &= \ln^2 (h/z_o) \\ b &= 9.4\ (h - z_o)\ \ln (h/z_o) - .74\ S\ \ln (h/z_o) \\ c &= \left[4.7\ (h - z_o)\right]^2 - 4.7\ (h - z_o)\ S\ . \end{aligned}\right\} \qquad (E.8)$$

It can be shown that (E.7) and (E.8) are reasonably well approximated by

$$\eta = \frac{.268\ R\ \ln (h/z_o)}{.287 - R}\ , \qquad (E.9)$$

in which

$$\left.\begin{aligned} R &\equiv 1.35\ h/S \\ \eta &\equiv h/L\ . \end{aligned}\right\} \qquad (E.10)$$

It is clear from (E.9) that L drops to zero as $R \to R_c \equiv .287$ and becomes negative for $R > R_c$. To avoid negative or zero L, we use Webb's profile laws for $\eta \geq 1$ (strong stability). The integrated forms are

$$F(L) = .74\ \ln (L/z_o) + \frac{6.35}{L}\ (L - z_o) + 7.35\ \ln \eta \qquad (E.11)$$

$$G(L) = \ln (L/z_o) + \frac{4.7}{L}\ (L - z_o) + 5.7\ \ln \eta\ . \qquad (E.12)$$

Numerical experiments show that the iterative solutions of (E.11), (E.12), and (2.14) converge quickly for $z_o \leq L \leq h$ and that L is well-behaved for $R > R_c$. Solutions for which $L < z_o$ are rejected as meaningless; L is equated to z_o.

Iterative solutions for L in unstable and strongly stable cases can be approximated by considerably simpler direct solutions. These solutions will be a subject of a future report.

APPENDIX F

LIST OF SYMBOLS (the number in parenthesis refers to the equation in which the symbol first appears or is defined):

A coordinate stretching parameter, $A = 152.43\ m^{-1}$, (2.1); A_j, B_j, C_j non-zero elements in a tri-diagonal system, (2.19); $A^e_{i,j}$ latest analysis estimate at gridpoint i,j, (4.4); $A^g_{i,j}$ analysis guess value, (4.4); $A^g(x,y)$ analysis estimate at any x,y point, (4.4)

C soil heat flux coefficient, (3.4) and Appendix C; C' soil heat flux term, (3.4) and Appendix C; C_w distance-dependent weight function (4.1); c_p specific heat capacity of air at constant pressure, (2.17)

D average station separation in number of grid units, (4.1); D_j known function of Q_j and its neighbors in tri-diagonal relation, (2.19)

E elevation, (3.8); evaporation, (3.3); $\mathcal{E}$ net energy at the surface, (3.5)

F integrated profile relation for potential temperature, (2.12); $F(\sigma^2)$ empirical statistical checking parameter, (4.2); $F_{i,j}$, $\overline{F}_{i,j}$, $\overline{F}_c$, F_x, F_y, $F_{x,y}$ filter grid values, (4.6-4.8); $F_{latent,sensible}$ latent and sensible heat fluxes, (3.1); f Coriolis parameter, (2.5)

G integrated profile relation for wind speed, (2.12); $\tilde{G}$ complex geostrophic wind vector, (2.5); g acceleration due to gravity, (2.10); g(z) measure of coordinate stretching (2.2); g(x,t) forcing function in advection equation, (D.1)

H height of the top of the BLM, (2.16); Halstead parameter for estimating evaporation, (3.3); h height of top of the surface layer, (2.1); $h_\pm$ distance from gridpoint j to gridpoint $j \pm 1$, (D.3); h_d height of the mixed depth, (2.17)

i,j,k indices for gridpoints, (2.1); $i = \sqrt{-1}$, (2.5)

$K_{T,m,q}$ turbulent diffusion coefficients for heat, momentum, and moisture, (2.3-5); k Von Karmen constant, k=.35, (2.10); K_h, K_H turbulent diffusion coefficient evaluated at z=h and H; $K_\pm$ turbulent diffusion coefficient evaluated at $z_\pm=(z_j+z_{j\pm1})/2$, (D.8)

L Obukhov length, (2.10); $\mathcal{L}$ latent heat of evaporation, (3.1)

M,N number of gridpoints in the x and y direction, (4.3)

$O(x,y)$ observed value, (4.4); O_i number of observations inside the grid, (4.3)

p pressure, (3.8)

Q_j arbitrary variable defined at gridpoint j, (2.19); Q_m data quality parameter for the m^{th} observation (4.4); q specific humidity, (2.4); q_* friction humidity, (3.2)

R influence radius, (4.1); R_c critical Richardson number, as defined by finite-difference values $\Delta U, \Delta\Theta$, (E.10), (2.13); R_{net} net radiation flux at the surface, excluding the upward long-wave flux, (3.5)

S $S(\sigma^2)$ empirical statistical checking parameter, (4.2)

T temperature, (3.4); $\tilde{T}$ complex temperature-humidity, (2.7) t elapsed time from initialization, (2.3)

u east-west wind component, (2.6); u_g east-west component of geostrophic wind (2.6); u_* friction speed, (2.10)

v north-south wind component, (2.6); v_g north-south component of geostrophic wind, (2.6); $\vec{V}$ three-dimensional wind vector, (2.4)

w vertical velocity (2.9); $\tilde{W}$ complex wind vector, (2.4); w_k filter weights, (4.5)

(x,y,z) eastward, northward, and local vertical grid coordinate (2.9), (2.1)

z' height in stretched coordinate system, (2.1); z_o surface roughness length, (2.12)

O^+, O^- limit of $O \pm \varepsilon$, as ε vanishes, (2.20)

Δ difference operator: ΔU and $\Delta\Theta$ are the differences in wind speed and potential temperature between z_o and h, (2.12); $\Delta t, \Delta x$, and Δz are increments in t, x, and z (2.1), (D.3); $\nabla\cdot$ three dimensional divergence (2.3); δ measure of smoothing in implicit filter, (2.20)

η non-dimensional reciprocal of Obukhov length, (E.10)

ε_s surface emissivity, (3.5)

Θ potential temperature, (2.3); Θ_* friction temperature, (2.10); $\bar{\Theta}$ average potential temperature in surface layer, (2.10)

ρ density of air, (3.1)

σ standard deviation, (4.2)

ϕ_T, ϕ_m, ϕ_q Monin-Obukhov universal functions for heat, momentum, and humidity, (2.10)

ω_n analysis weight function for the nth observation, (4.5).

(Continued from inside front cover)

WBTM TDL 33 Calculation of Precipitable Water. L. P. Harrison, June 1970, 61 pp. (PB-193-600)

WBTM TDL 34 An Objective Method for Forecasting Winds Over Lake Erie and Lake Ontario. Celso S. Barrientos, August 1970, 20 pp. (PB-194-586)

WBTM TDL 35 Probabilistic Prediction in Meteorology: a Bibliography. Allan H. Murphy and Roger A. Allen, June 1970, 60 pp. (PB-194-415)

WBTM TDL 36 Current High Altitude Observations--Investigation and Possible Improvement. M. A. Alaka and R. C. Elvander, July 1970, 24 pp. (COM-71-00003)

NOAA Technical Memorandums

NWS TDL 37 Prediction of Surface Dew Point Temperatures. R. C. Elvander, February 1971, 40 pp. (COM-71-00253)

NWS TDL 38 Objectively Computed Surface Diagnostic Fields. Robert J. Bermowitz, February 1971, 23 pp. (COM-71-00301)

NWS TDL 39 Computer Prediction of Precipitation Probability for 108 Cities in the United States. William H. Klein, February 1971, 32 pp. (COM-71-00249)

NWS TDL 40 Wave Climatology for the Great Lakes. N. A. Pore, J. M. McClelland, C. S. Barrientos, and W. E. Kennedy, February 1971, 61 pp. (COM-71-00368)

NWS TDL 41 Twice-Daily Mean Monthly Heights in the Troposphere Over North America and Vicinity. August F. Korte, June 1971, 31 pp. (COM-71-00826)

NWS TDL 42 Some Experiments With a Fine-Mesh 500-Millibar Barotropic Model. Robert J. Bermowitz, August 1971, 20 pp. (COM-71-00958)

NWS TDL 43 Air-Sea Energy Exchange in Lagrangian Temperature and Dew Point Forecasts. Ronald M. Reap, October 1971, 23 pp. (COM-71-01112)

NWS TDL 44 Use of Surface Observations in Boundary-Layer Analysis. H. Michael Mogil and William D. Bonner, March 1972, 16 pp. (COM-72-10641)

NWS TDL 45 The Use of Model Output Statistics (MOS) To Estimate Daily Maximum Temperatures. John R. Annett, Harry R. Glahn, and Dale A. Lowry, March 1972, 14 pp. (COM-72-10753)

NWS TDL 46 SPLASH (Special Program To List Amplitudes of Surges From Hurricanes): I. Landfall Storms. Chester P. Jelesnianski, April 1972. 52 pp. (COM-72-10807)

NWS TDL 47 Mean Diurnal and Monthly Height Changes in the Troposphere Over North America and Vicinity. August F. Korte and DeVer Colson, August 1972, 30 pp. (COM-72-11132)

NWS TDL 48 Synoptic Climatological Studies of Precipitation in the Plateau States From 850-, 700-, and 500-Millibar Lows During Spring. August F. Korte, Donald L. Jorgensen, and William H. Klein, August 1972, 130 pp. (COM-73-10069)

NWS TDL 49 Synoptic Climatological Studies of Precipitation in the Plateau States From 850-Millibar Lows During Fall. August F. Korte and DeVer Colson, August 1972, 56 pp. (COM-74-10464)

NWS TDL 50 Forecasting Extratropical Storm Surges For the Northeast Coast of the United States. N. Arthur Pore, William S. Richardson, and Herman P. Perrotti, January 1974, 70 pp. (COM-74-10719)

NWS TDL 51 Predicting the Conditional Probability of Frozen Precipitation. Harry R. Glahn and Joseph R. Bocchieri, March 1974, 33 pp. (COM-74-10909)

NWS TDL 52 SPLASH (Special Program to List Amplitudes of Surges From Hurricanes): Part Two. General Track and Variant Storm Conditions. Chester P. Jelesnianski, March 1974, 55 pp. (COM-74-10925)

NWS TDL 53 A Comparison Between the Single Station and Generalized Operator Techniques for Automated Prediction of Precipitation Probability. Joseph R. Bocchieri, September 1974, 20 pp. (COM-74-11763)

NWS TDL 54 Climatology of Lake Erie Storm Surges at Buffalo and Toledo. N. Arthur Pore, Herman P. Perrotti, and William S. Richardson, March 1975, 27 pp. (COM-75-10587)

NWS TDL 55 Dissipation, Dispersion and Difference Schemes. Paul E. Long, Jr., May 1975, 33 pp.(COM-75-10972)

NWS TDL 56 Some Physical and Numerical Aspects of Boundary Layer Modeling. Paul E. Long, Jr. and Wilson A. Shaffer, May 1975, 37 pp. (COM-75-10980)

NWS TDL 57 A Predictive Boundary Layer Model. Wilson A. Shaffer and Paul E. Long, Jr., May 1975, 44 pp. (PB-265-412)

NWS TDL 58 A Preliminary View of Storm Surges Before and After Storm Modifications for Alongshore-Moving Storms. Chester P. Jelesnianski and Celso S. Barrientos, October 1975, 16 pp. (PB-247-362)

NWS TDL 59 Assimilation of Surface, Upper Air, and Grid-Point Data in the Objective Analysis Procedure for a Three-Dimensional Trajectory Model. Ronald M. Reap, February 1976, 17 pp. (PB-256-082)

NWS TDL 60 Verification of Severe Local Storm Warnings Based on Radar Echo Characteristics. Donald S. Foster, June 1976, 9 pp. plus supplement. (PB-262-417)

NWS TDL 61 A Sheared Coordinate System for Storm Surge Equations of Motion With a Mildly Curved Coast. Chester P. Jelesnianski, July 1976, 52 pp. (PB-261-956)

NWS TDL 62 Automated Prediction of Thunderstorms and Severe Local Storms. Ronald M. Reap and Donald S. Foster, April 1977, 20 pp. (PB-268-035)

NWS TDL 63 Automated Great Lakes Wave Forecasts. N. Arthur Pore, February 1977, 13 pp. (PB-265-854)

NWS TDL 64 Operational System for Predicting Thunderstorms Two to Six Hours in Advance. Jerome P. Charba, March 1977, 24 pp. (PB-266-969)

NWS TDL 65 Operational System for Predicting Severe Local Storms Two to Six Hours in Advance. Jerome P. Charba, May 1977, 36 pp. (PB-271-147)

NOAA--S/T 78-115